Mechanisms Responsible for Microwave Properties in High Performance Dielectric Materials

by

Shengke Zhang

A Dissertation Presented in Partial Fulfillment
of the Requirements for the Degree
Doctor of Philosophy

Approved April 2016 by the
Graduate Supervisory Committee:

Nathan Newman, Chair
Terry L. Alford
Ralph Chamberlin
Marco Flores
Rakesh K. Singh

ARIZONA STATE UNIVERSITY

May 2016

ABSTRACT

Microwave properties of low-loss commercial dielectric materials are optimized by adding transition-metal dopants or alloying agents (i.e. Ni, Co, Mn) to tune the temperature coefficient of resonant frequency (τ_f) to zero. This occurs as a result of the temperature dependence of dielectric constant offsetting the thermal expansion. At cryogenic temperatures, the microwave loss in these dielectric materials is dominated by electron paramagnetic resonance (EPR) loss, which results from the spin-excitations of d-shell electron spins in exchange-coupled clusters. We show that the origin of the observed magnetically-induced shifts in the dielectric resonator frequency originates from the same mechanism, as described by the Kramers-Kronig relations. The temperature coefficient of resonator frequency, τ_f, is related to three material parameters according to the equation, $\tau_f = -(½\ \tau_\varepsilon + ½\ \tau_\mu + \alpha_L)$, where τ_ε, τ_μ, and α_L are the temperature coefficient of dielectric constant, magnetic permeability, and lattice constant, respectively. Each of these parameters for dielectric materials of interest are measured experimentally. These results, in combination with density functional simulations, developed a much improved understanding of the fundamental mechanisms responsible for τ_f. The same experimental methods have been used to characterize *in-situ* the physical nature and concentration of performance-degrading point defects in the dielectrics of superconducting planar microwave resonators.

ACKNOWLEDGMENTS

First and foremost I would like to express my greatest gratitude to my advisor, Prof. Nathan Newman. I extremely appreciate all his “screaming and yelling”, “constant communication and meetings”, “daily report”, and “superuser rule” to not only make my doctoral education experience productive and invigorating, but also shape me into a better researcher and leader. As a matter of fact, Prof. Newman is the first professor I met at ASU 6 years ago in the MSE 482 class when I was a 21-year-old just arrived at United States who did not understand 80 % of his jokes in that class; 6 years later, he will be the last professor I say farewell to with a doctoral degree and a decent job with multiple offers. Life is a dramatic show as it came to a full circle. The joy and enthusiasm, the tears and anxiousness intertwined over the last four years, was motivational and contagious for me, and will be one of the most unforgettable memories in my life.

My profound gratitude also extends to all my doctoral committee members, Prof. Terry Alford, Prof. Ralph Chamberlin, Prof. Marco Flores, and Prof. Rakesh Singh for providing me with their generous time and advice to evaluate my work and better my thesis.

Every result described in this thesis was accomplished with the help and support of fellow lab-mates and collaborators. I am grateful for having had the opportunity to work with a team of wonderful colleagues throughout this journey in Newman research group. In no particular order, these are Dr. Lingtao Liu, Dr. Mahmoud Vahidi, Dr. Lei Yu, Dr. Mengchu Huang, Dr. Shaojun Liu, Dr. Brett Strawbridge, Dr. Zhizhong Tang, Dr. Nick Rizzo, Dr. John Rowell, Richard Hanley, Scott Ageno, Cameron Kopas, Siddhesh Gajare, Justin Gonzales, Dengfeng Tao, Makram Qader, Aditya Ravi, Aditya

Walimbe, Chinnu Merin Abraham, Pu Han, Alex Wertheim, You Li, Cougar Garcia, Andrew Shurman, Thomas Chamberlin, Brooke Hudson, and Adam Pocock; also, three wonderful high school students who I worked closely with, Rohit Badia, Sejal Aggarwal, and Alex Stoken.

Furthermore, I would like to acknowledge Dr. Marco Flores for his help, guidance, and challenges on electron paramagnetic resonance (EPR), Dr. Hassan Sahin and Dr. Sefaattin Tongay for the first-principles calculations, Dr. Neil Dilley, Dinesh Martien, and Tyler DaPron for the dilatometer measurements at Quantum Design, and all the support provided by LeRoy Eyring Center for Solid State Science at Arizona State University.

Moreover, I also appreciate all the scientific discussions and support from Dr. Daniel Queen and Dr. Brian Wagner. I believe we will continue our productive and fruitful collaboration on the superconducting microwave resonator project.

My time at ASU was made enjoyable in large part due to the many friends that became an integral part of my life. In many ways, they have contributed immensely to my personal and professional growth. I am grateful for time spent with Dr. Haobo Chen, Dr. Chengwei Wang, Ting Yang, Chengchen Guo, Jie Ding, Weixiao Li, Jingxian Mao, Shaoshi Huan, Rouhan Zhang, Qian Cheng at the SRC playing basketball, swimming, snowboarding, workout, hanging out, or dining on/off campus throughout the pursuit of my doctoral degree.

A very special acknowledgement goes to my fiancée, Fei Gao, who has offered her companionship, love, and inspirations throughout my doctoral journey. We have been together for four and half years when I was drafting this thesis. We met at ASU six year

ago, but we didn't know we went to the same high school and university back in China. What a small world! A lot have happened in our life, and a lot more will be happening in our future. We have had two years long-distance relationship. It was hard, but it worked. In a month or two, I will be moving to your city, and a new chapter of our life is about to begin. I am extremely excited about the joys and adventures ahead of us. I am so lucky to have met you here.

Finally, I would like to dedicate this thesis to my parents, Bin Zhang and Yongping Zhang, who support me, encourage me, and love me from a long, long distance away. I feel really guilty that I did not spend enough time with you over the last 6 years. Thanks mom and dad for everything you have done for me. I will do all I can to make you proud.

TABLE OF CONTENTS

Page

LIST OF TABLES

Table Page

LIST OF FIGURES

Figure Page

1. INTRODUCTION

Ceramic $Ba(Zn_{1/3}Ta_{2/3})O_3$ (BZT) and $Ba(Zn_{1/3}Nb_{2/3})O_3$ (BZN) temperature-compensated microwave dielectrics are used extensively in military and civilian microwave communication and Doppler radar systems [1-4]. Commercial manufacturers of BZT and BZN ceramics introduce "magnetic" transition-metal additives, such as Co, Ni and Mn, in these materials to improve their manufacturability and tune their temperature coefficient of resonant frequency, τ_f. Despite their widespread use of these transition-doped perovskites, the mechanisms that are responsible for the microwave loss and τ_f are not yet fully understood.

To date, researchers have identified a number of mechanisms that can cause microwave loss in dielectrics, including free carrier and polaron conduction [5-7], EPR [4, 8-9], anharmonic-phonon [10-12], and precession of electric dipoles in polar molecules [13].

In chapter 2, I carried out a systematic study to investigate the role of Co, Mn, and Ni on BZT's and BNT's loss tangent (tan δ), relative dielectric constant (ε_r), and relative magnetic permeability (μ_r) as a function of additive concentration, magnetic field (0 - $9x10^4$ G) and temperature (4-300 K). This work also demonstrated that the use of optimal material selection could be used to make ultra-high Q passive microwave devices with externally controlled transfer functions, as the quality factor (Q) of the composition $Ba(Co_{1/15}Zn_{4/15}Nb_{2/3})O_3$ at 77 K can be tuned from 1,100 to 12,000 at 10 GHz through the application of practical magnetic fields.

Chapter 3 focuses the discussion on the fundamental mechanisms that determine the temperature coefficient of resonant frequency (τ_f) in high performance microwave

dielectrics. The resonant frequency of dielectric resonators is determined by the dimensions (L), dielectric constant (ε), and permeability (μ). The temperature dependence of these three parameters causes a "drift" of resonant frequency, as τ_f follows: $\tau_f = -(\frac{1}{2}\tau_\varepsilon + \frac{1}{2}\tau_\mu + \alpha_L)$, where τ_ε is the temperature coefficient of dielectric constant, τ_μ is the temperature coefficient of magnetic permeability, and α_L is the thermal expansion of the lattice. In this chapter, I determined the τ_ε by individually characterizing α_L, τ_f, and τ_μ from cryogenic temperatures up to room temperature. We also performed first-principles simulations of BNT and BZT to gain a fundamental understanding of the mechanisms responsible for the observed temperature dependence of these parameters.

In chapter 4 of this thesis, I report my investigation of the physical nature and concentration of performance-degrading point defects in the dielectrics of superconducting planar microwave resonators. The performance of these devices is limited by dielectric and metal losses [14-18]. These superconductor configurations have been utilized in a wide range of applications including kinetic inductance detectors (KID) [19-20], quantum memory [21-23], superconductor logic circuits [24], and quantum circuits [25]. To identify and quantify the performance-degrading defects in the dielectric layers, I developed a novel *in-situ* electron paramagnetic resonance (EPR) spectroscopy using superconducting parallel plate and stripline resonators. I discuss the design, simulation, fabrication, material selections, and realization of this *in-situ* EPR technique. Then, I investigate the properties of defects in a conventional high purity semiconductor by utilizing this technique. The limitation of the technique is also discussed. Chapter 5 summarizes this thesis.

2. MAIN SOURCE OF MICROWAVE LOSS IN TRANSITION-METAL-DOPED DIELECTRIC RESONATOR AT CRYOGENIC TEMPERATURES

2.1 Introduction

"Magnetic" transition-metal additives (i.e. Co, Mn, and Ni) are commonly added into high performance microwave ceramics $Ba(Zn_{1/3}Ta_{2/3})O_3$ (BZT) and $Ba(Zn_{1/3}Nb_{2/3})O_3$ (BZN) by commercial manufacturers to tune the temperature dependence of resonant frequency (τ_f). An understanding of the dominant loss mechanism at temperatures below room temperature is lacking and is the focus of our recent studies.

In this chapter, we report the results of temperature dependent and magnetic dependent microwave loss measurements on dielectrics in order to investigate the dominant loss mechanism at cryogenic temperatures. The transition-metal additives of interest are Co^{2+} and Ni^{2+} ions whose electronic states have a large angular momentum (L = 3) and Mn^{2+} ions that do not (L = 0). Also, experiments and Kramers-Kronig simulations were performed to determine if relationship of the loss tangents and changes in magnetic susceptibility can be attributed to a common mechanism, spin excitations. Lastly, we showed that the microwave performance of Co-doped BZN can be tuned by a factor of 10 or more at 10 GHz by applying of practical magnetic fields (i.e. < 1 Tesla) at 77 K.

2.2 Dielectric Microwave Resonators

2.2.1 High-performance Microwave Dielectric Materials Synthesis and Characterization

2.2.1.1 High Quality Dielectric Materials Synthesis

Dielectric $Ba(Zn_{1/3}Ta_{2/3})O_3$ (BZT) and $Ba(Zn_{1/3}Nb_{2/3})O_3$ (BZN) resonators studied in this work are all synthesized by using conventional ceramic powder processing methods in our lab [26]. The ceramics with the various additives were made from reagent grade $BaCO_3$ (99.9%, Strem Chemicals), ZnO (99.9%, Alfa Aesar), Ta_2O_5 (99.99%, H. C. Starck), Nb_2O_5 (99.9%, Signa-Aldrich), MnO_2 (99.9%, Alfa Aesar), NiO (99.99% Strem Chemicals) and Co_3O_4 (99.9%, Spectrum Chemical) powders. To synthesize the ceramics, the raw materials are blended using ball milling to de-agglomerate the powders and provide a homogeneous distribution of raw materials. The slurry are then dried and subsequently calcined at 1250 ^oC for 10 hours. After the reaction step, the BZT powders are ball-milled in aqueous slurry with polyvinyl alcohol-poly ethylene glycol binder to reduce the particle size to that suitable for sintering; the BZN powders are ball-milled in aqueous slurry with paraffin wax-stearic acid mix binder to reduce the particle size to that suitable for sintering. The resulting slurries are dried, filtered through a 48-mesh screen, and then pressed to ~60% of theoretical density. The BZT green-body pucks are heated to 1550 °C for 16 hours in air in a box furnace to form single-phase materials. The green-body BZN pucks are heated to 1450°C for 16 hours in air in a box furnace to form single-phase materials. The BZT and BZN are covered with calcined powders and placed in an alumina crucible during sintering.

In this alloy system, Zn, Ni, Mn, and Co share the common B' site in the $A(B'_{1/3}B''_{2/3})O_3$ complex perovskite structure. The following compositions were produced using these methods. $Ba((Zn_{1-x}Mn_x)_{1/3}Ta_{2/3})O_3$ with the Mn faction, x, of $0.0075<x<0.12$, $Ba((Zn_{1-x}Co_x)_{1/3}Ta_{2/3})O_3$ and $Ba((Zn_{1-x}Co_x)_{1/3}Nb_{2/3})O_3$ with the Co fraction, x, of $0.06<x<0.60$, and $Ba((Zn_{0.88}(Mn_xNi_{1-x})_{0.12})_{1/3}Ta_{2/3})O_3$ with x=0, 0.166, 0.50, 0.833. For

brevity, we denote the composition of BZT and BZN alloys by the fraction of additives on the B' site henceforth. The mole fraction % can be quickly determined, as the Zn site represents one of 15 atomic sites in the unit cell, so the mole fraction is equal to the fraction of impurities on the Zn site (i.e. x) divided by 15.

2.2.1.2 Dielectric Material Structural and Magnetic Property Characterization

The chemical compositions of the ceramic samples were verified by particle induced X-ray emission (PIXE).

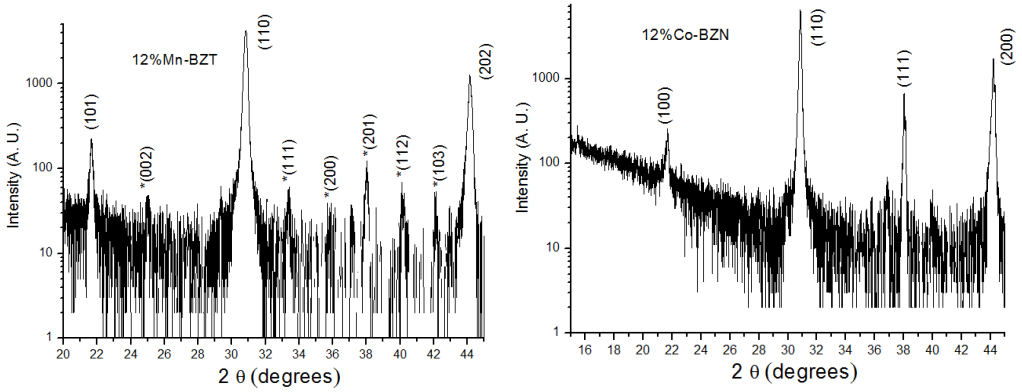

Figure 2. 1 XRD Results of 12% Mn-doped BZT and 12% Co-doped BZN from 20 to 43 Degrees. 12% Mn-BZT Shows A Lot of Superlattice Peaks, But 12% Co-BZN Does Not Show Any Significant Superlattice Peaks.

X-ray diffraction (XRD) results in figure 2.1 showed that all the mixed solutions form miscible solid solution, and no secondary phases were observed. XRD results found that the BZT samples were hexagonal with 1:2 ordering on the B'B'' site [27]. XRD results from BZN samples showed no hexagonal-structured superlattice peaks, indicating a disordered pseudo-cubic structure.

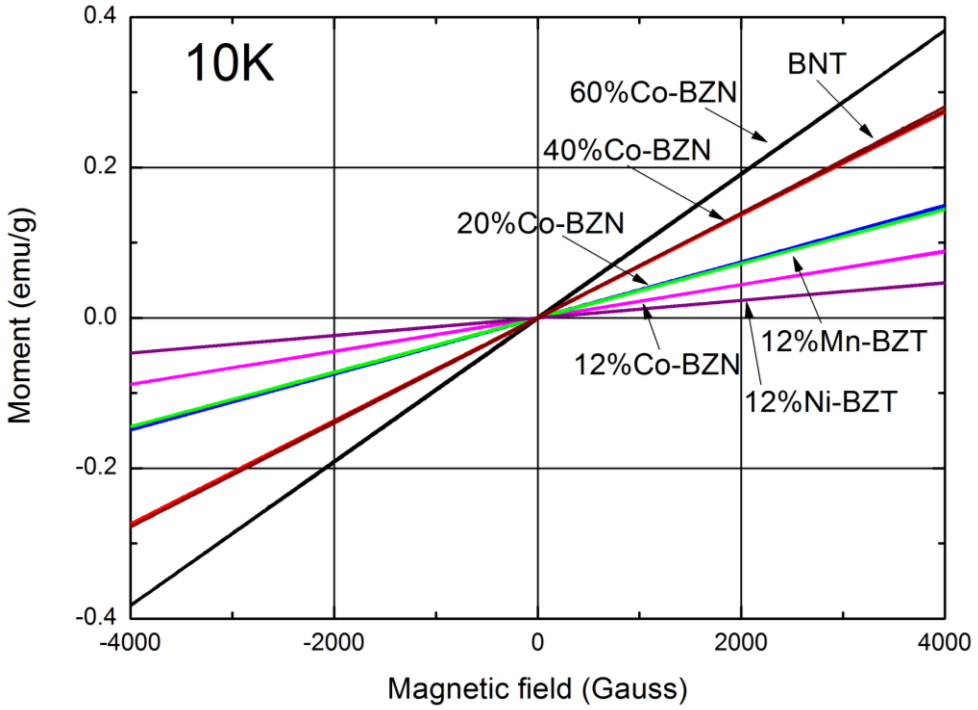

Figure 2. 2 Measurements of Magnetic Field as A Function of Magnetization in Microwave Dielectrics with Different Transition-metal Contents and Doping Concentration at 10 K. Data Shows That Samples Do Not Contain A Ferromagnetic Secondary Phase As Low As 10 K.

Magnetic susceptibility determinations (figure 2.2) were performed using a vibrating sample magnetometer (VSM) Quantum Design PPMS system (Model 6000, Quantum Design, San Diego, CA). Ni, Co, and Mn samples spanning the range of doping concentrations investigated in this study were found to exhibit antiferromagnetic characteristics with Weiss temperatures of less than 7 K. Scans of the sample moment as a function of magnetic field at ~10 K were found to be linear and non-hysteretic, indicating that the samples do not contain a ferromagnetic secondary phase.

2.2.2 Dielectric Resonators Measurement Technique

2.2.2.1 High Frequency Structural Simulator (HFSS) Simulation of Dielectric Resonator (DR) Technique

HFSS (ANSYS) microwave simulation software is used to design, simulate, and verify microwave dielectric resonator measurements in this thesis. HFSS is a highly efficient electromagnetic (EM) field simulator that employs the finite element method, adaptive meshing, and brilliant visualization for 3D volumetric passive devices modeling.

Firstly, I designed and simulated a 2.03 cm x 0.61 cm x 1.52 cm copper (Cu) cavity, whose conductivity is designed to be 5.8×10^7 Siemens/m, a typical value for Cu at 20 °C [28]. The HFSS simulation finds 11.99 GHz and 15.82 GHz as the first and second order modes of the Cu cavity, which match fairly well with the measured cavity resonant frequencies at 11.50 GHz and 15.35 GHz at room temperature, respectively. The simulated electric field patterns in the magnitude and vector forms of these two modes are shown in figure 2.3 a and b. Figure 2.3 (a) shows that the maximum electric fields are observed at the center of the cavity in the form of red rings, and minimum electric fields are present near the edges in the form of blue rings. As plotting the electric field in vector form in figure 2.3 (b), the contour of the electric field vectors forms a half wavelength pattern. Since there are not electric fields travelling in the longitudinal direction (parallel to the coaxial cables), this resonance mode is designated as a TE_{101} mode. In figure 2.3 (c), the electric fields of the second resonance at 15.82 GHz show 2 maxima and 3 minima, indicating a full wavelength mode. The vector electric fields plotted in figure 2.3 (d) are the characteristic of a full wavelength pattern with a mode index of TE_{102}.

The resonant frequencies of a rectangular metal cavity can be calculated using the following equation [29],

$$f_{mnl} = \frac{ck_{mnl}}{2\pi\sqrt{\varepsilon_r\mu_r}} = \frac{c}{2\pi\sqrt{\varepsilon_r\mu_r}}\sqrt{(\frac{m\pi}{a})^2+(\frac{n\pi}{b})^2+(\frac{l\pi}{c})^2} \quad \text{Equation (2.1)}$$

where k_{mnl}=wavenumber, m, n, l are mode numbers, and a, b, d are corresponding dimensions.

When an 8.5 mm x 6 mm x 2 mm dielectric resonator (DR) with dielectric constant of 30 is placed in the Cu cavity, HFSS simulations find the fundamental resonant frequency to be at 9.67 GHz. The measured resonant frequencies of BZT and Ni-doped BZT samples are seen in the range of 9.5 – 10 GHz. Thus, the measured and simulated resonant frequency agrees to within 5%.

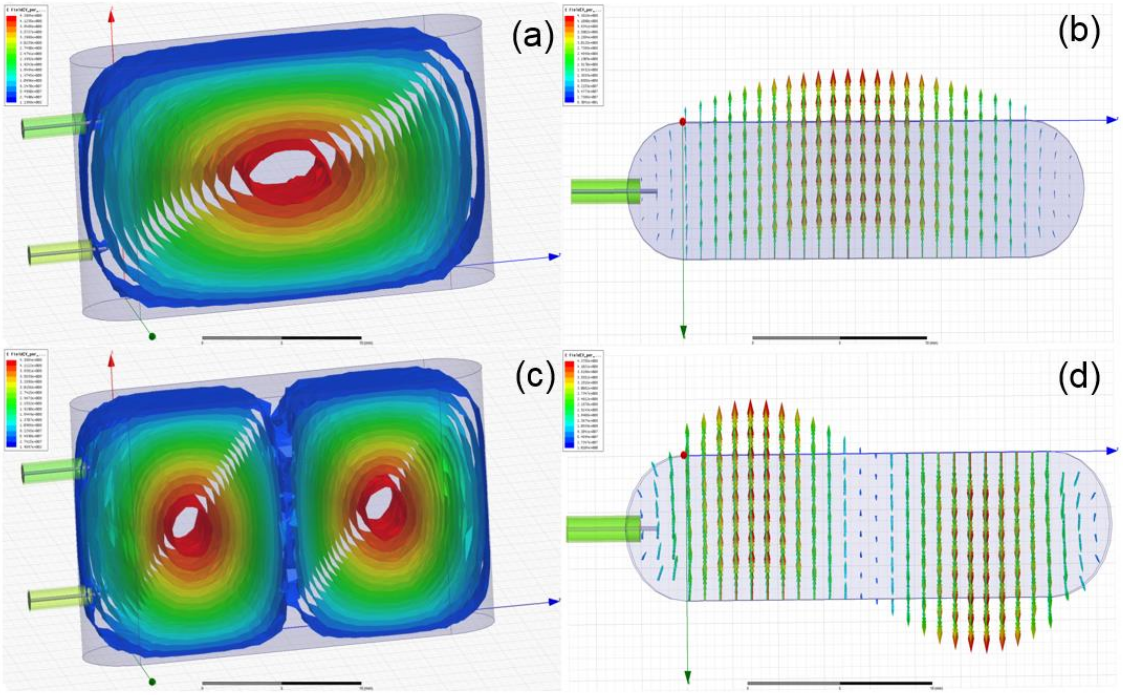

Figure 2. 3 Electric Field in the Magnitude and Vector Form for TE_{101} and TE_{102} Cu Cavity Resonant Modes.

The electric field of the DR at 9.67 GHz is plotted in figure 2.4. The pattern is characterized by a single minimum at the center of the cavity and maxima at the edges, characteristic of the product of half wavelength patterns in both the x- and y- directions. The vector electric fields, illustrated in figure 2.4 (b), are found to circulate in a clockwise direction from this viewpoint. The magnetic fields are found to oscillate in the transverse plane. This is designated as a $TE_{11\delta}$ mode [30-31].

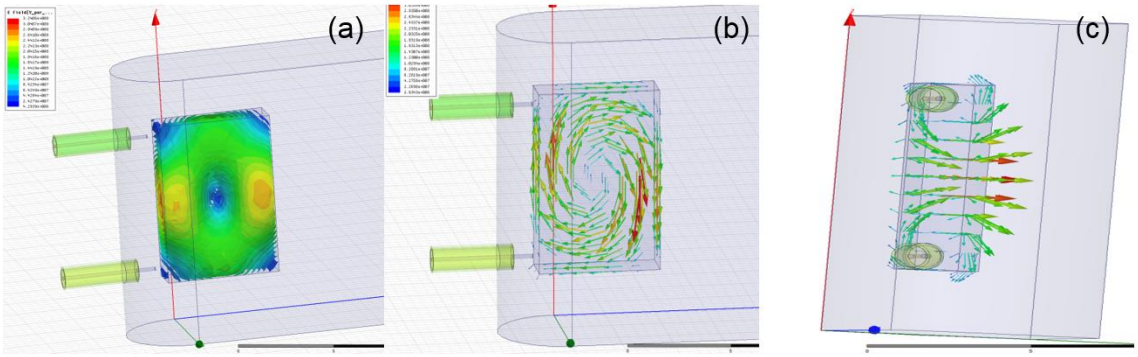

Figure 2. 4 (a) and (b) The Electric Field in the Magnitude and Vector Form for TE_{101} Mode of (c) The Magnetic Field in Vector Form for TE_{101} Resonant Mode.

2.2.2.2 The Magnetic Field and Temperature Dependent Loss Tangent Measurement Technique

The loss tangents of dielectric materials are determined using microwave dielectric resonator (DR) measurements [4, 9, 32]. The 8.5 mm x 6.5 mm x 2mm rectangular DRs are inserted into a 2.03 cm x 0.61 cm x 1.52 cm gold-plated copper cavity which is affixed to the end of a cryogenic dipping probe. See figure 2.5. An HP8510C microwave vector network analyzer is used to measure S_{21} vector transmission values. The microwave signals to and from the copper cavity are transmitted through 50 Ω semi-rigid coaxial cables (silver plated copper inner conductor, stainless steel outer conductor, 50 Ω, 4.8 dB/m attenuation @10GHz, UT-085-SS, Micro Coax, Pottstown, PA). The microwave electric field coupling probes are fabricated by stripping back the wire at the end of the coax probes. Micrometers and their associated clamps grip and move the coaxial cable so that the distance between the microwave coupling probes and sample results in a measurable signal that is weakly coupled to the resonator. This allows the unloaded Q of the dielectric resonator to be determined to better than a few percent.

For measurements at temperatures from 2 to 400 K and magnetic fields as high as 9 Tesla, the microwave cavity is lowered into a cryostat (PPMS, Model 6000, Quantum Design, San Diego, CA). A LabVIEW (National Instruments, Austin, TX) program is used to set the magnetic field and temperature range, step, and rate in the PPMS, and then initiate the microwave measurements and record S_{21} values from the HP8510C microwave vector network analyzer. These values are then fit to a circle in the Smith chart using a MATLAB script inserted into the LabVIEW computer module to infer the Q [33]. The microwave dipping probe cavity and methods were originally developed to characterize superconductor films and resonators and are described in reference 34-36. The agreement between DR and superconducting parallel plate resonator (PPR) measurements of the loss tangent of dielectrics validates this technique [32, 34-37].

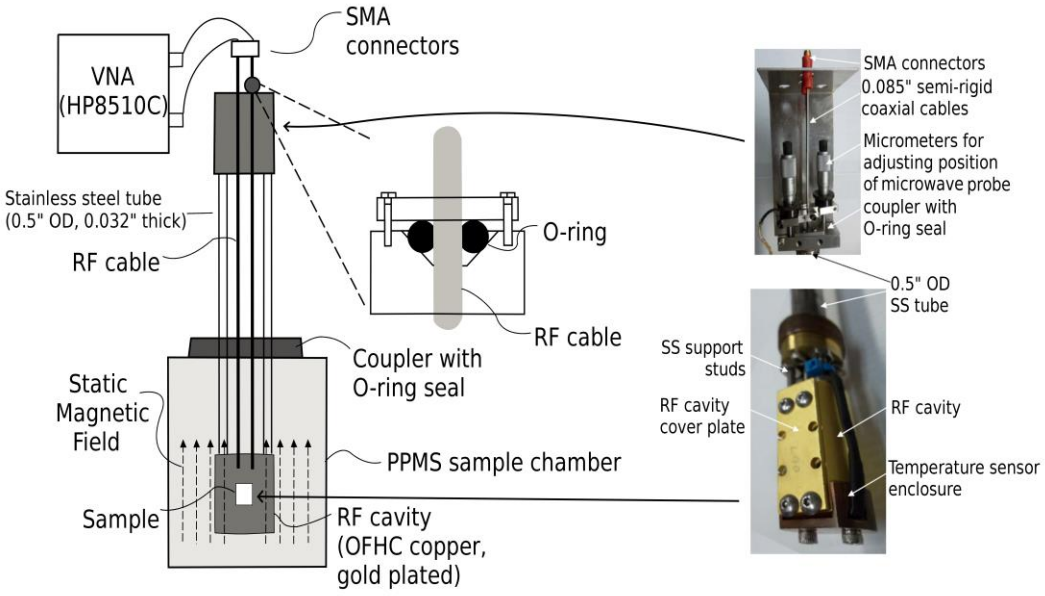

Figure 2. 5 Schematic (Left) and Pictures of Microwave Probe Position Adjusters (Top Right) and Gold-plated Cu Microwave Cavity (Bottom Right) for Measuring the Loss Tangent and EPR Spectra of Small Dielectric Samples Over A Range of Temperatures and Magnetic Fields.

2.3 Introduction to Electron Paramagnetic Resonance (EPR)

Electron paramagnetic resonance (EPR) spectroscopy is a technique to characterize the electronic properties of the unpaired electrons through their spins in the materials of interest. Every unpaired electron has a spin quantum number s=1/2 with magnetic components of m_s = +1/2 and m_s = -1/2. When there is no external magnetic field applied, the electron spins are randomly oriented. When an external magnetic field, B_{ex}, is present, the electron spins start precessing around the external magnetic field direction and the energy levels are split due to Zeeman effect, as mathematically expressed in the following equation,

$$\Delta E=\mu_B g B_{ex} \qquad \text{Equation (2.2)}$$

where μ_B is Bohr magnetron, 9.274 x 10^{-24} J/T, g is the Lande g-factor, and B_{ex} is the external magnetic field.

The EPR resonance takes when an incident microwave photon has the same energy as the Zeeman energy, as shown in figure 2.6 and mathematically defined in the following equation.

$$h\nu = \mu_B g B_{ex} \qquad \text{Equation (2.3)}$$

where *h* is the Planck constant, 6.62607 x 10^{-34} J/s, and ν is the frequency.

Physically, the electrons undergo a “spin-flip” process from the lower energy state to the higher energy state.

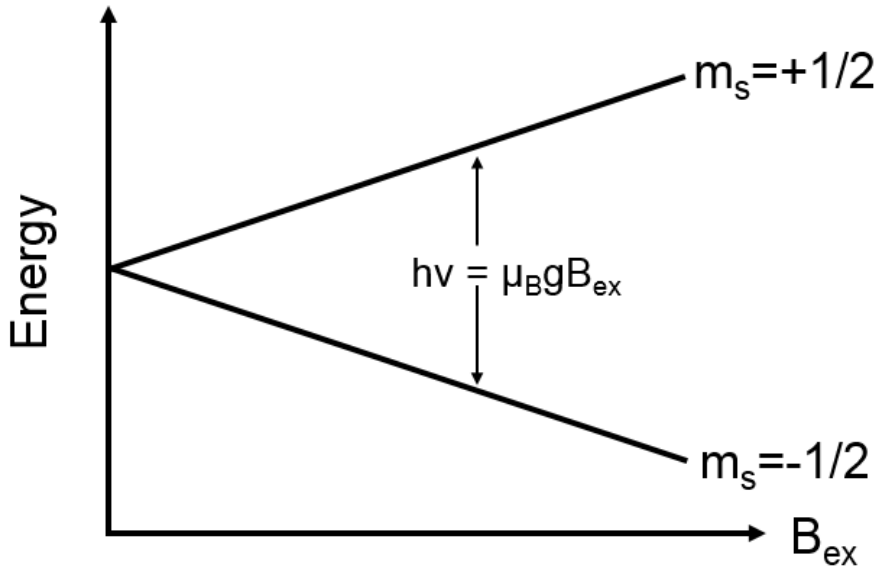

Figure 2. 6 Energy Diagram for EPR Absorption Process of S = 1/2.

The spin Hamiltonian of an EPR absorption process can be written as,

$$\mathrm{H} = \mu_B g\, \mathbf{B} \cdot \mathbf{S} + h\, \mathbf{S} \cdot \mathbf{D} \cdot \mathbf{S} + h\, \mathbf{S} \cdot \mathbf{A} \cdot \mathbf{I}$$

Equation (2.4)

The first term is the Zeeman effect. The second term shows the zero field splitting (ZFS) effect, which is only considered when the ZFS parameters D and/or E are no longer zero, and the material system has more than one unpaired electron (s > 1/2). The last term is the interaction between electron and nuclear spin magnetic moments, which is also called hyperfine splitting.

2.4 EPR Losses from the Transition-Metal Additives in $Ba(Zn_{1/3}Ta_{2/3})O_3$ (BZT) and $Ba(Zn_{1/3}Nb_{2/3})O_3$ (BZN) Dielectric Materials

2.4.1 Magnetic Field Dependence of Losses in Mn-doped BZT

Figure 2.7 shows the magnetic field dependence of loss tangent and $\varepsilon_r\mu_r$ from 50 K to 300 K. The major peak that is centered at ~3350 G is attributed to EPR from the Mn^{2+} $3d^5$ ($^6S_{5/2}$). This resonant value corresponds to an electron gyromagnetic ratio of 2.01 ± 0.01, very near that of a free electron.

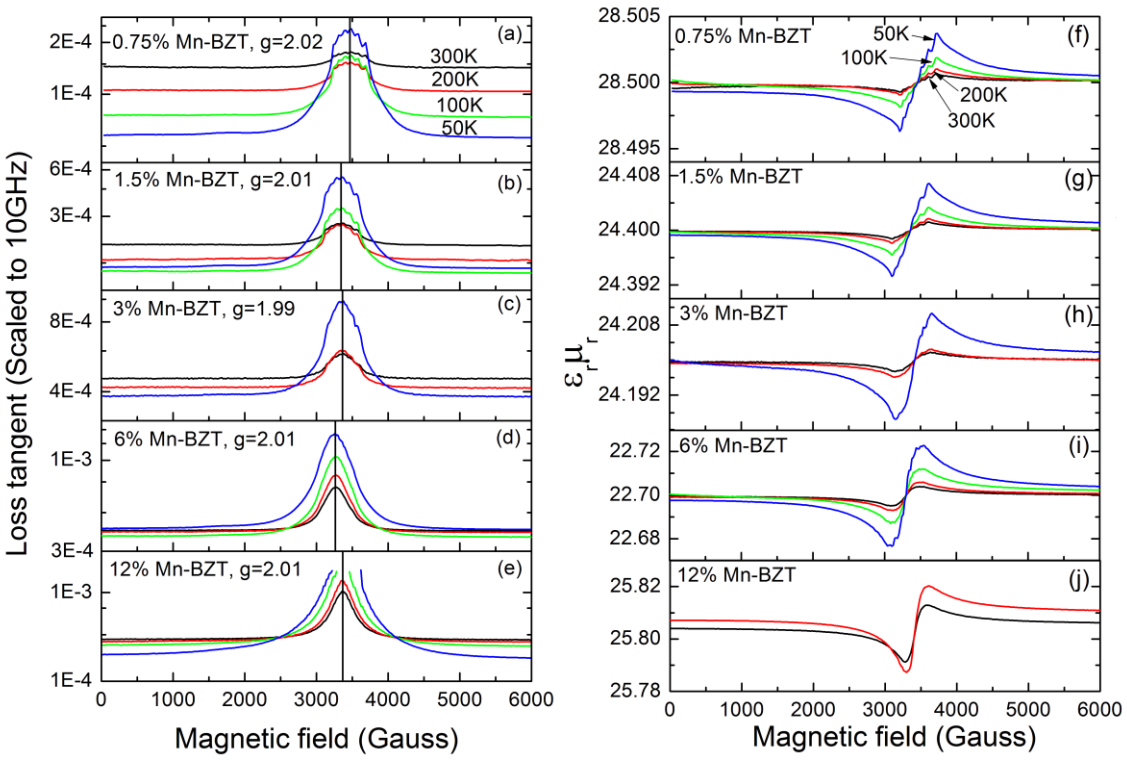

Figure 2. 7 Magnetic Field Dependence of Loss Tangent (a-e) and $\varepsilon_r\mu_r$ (f-j) of 0.75%, 1.5%, 3%, 6%, and 12% Mn-doped BZT for Temperatures at 50 K (blue-line), 100 K (Green-line), 200 K (Red-line), and 300 K (Black-line); For Measurements on 12% Mn Below 200 K, Reliable Measurements Could Not Be Made At or Near Resonance Due To the High Loss Under These Conditions and Therefore These Values Are Missing in the Figure.

Six hyperfine peaks are observed, which are most prominent in 0.75% Mn-doped BZT sample, due to the nuclear magnetic moments of the Mn^{2+} I = $^5/_2$ nuclei (i.e. m_I = -$^5/_2$, -$^3/_2$, -$^1/_2$, +$^1/_2$, +$^3/_2$, +$^5/_2$). At higher Mn concentrations, the influence of dipolar broadening, resulting from the differing magnetic environments of neighboring ions, washes out the hyperfine features.

The loss tangent peak intensities are larger at low temperatures than at elevated temperatures because of two factors; (1) the statistical Boltzmann population difference between the lower and upper Zeeman level; (2) the T_1 (spin-lattice) and T_2 (spin-spin) lifetimes are longer.

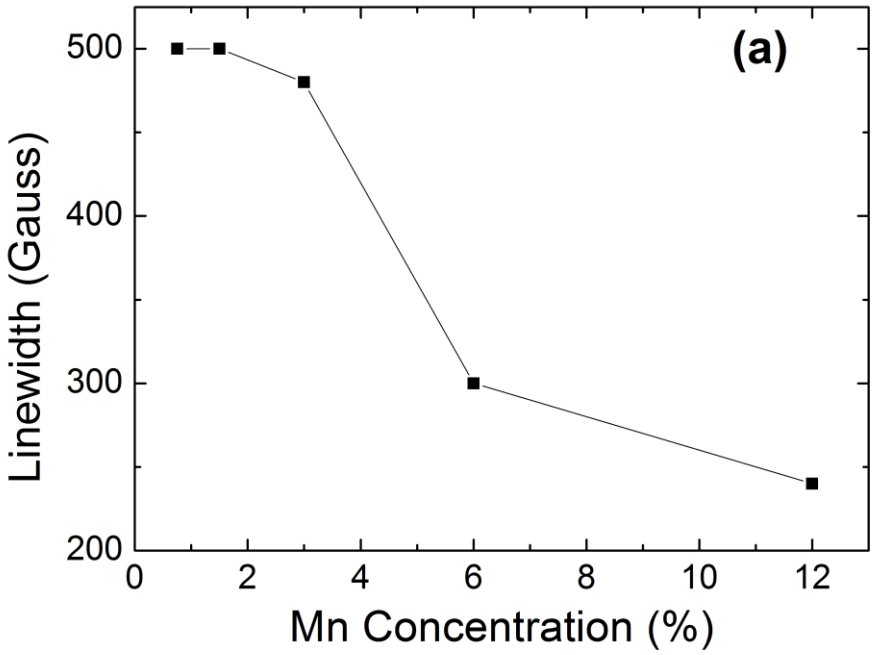

Figure 2. 8 Linewidth of The g = 2.01 Mn^{2+} EPR Loss Tangent Peak (~3350 Gauss) at 300 K.

The linewidth of the Mn resonance decreases with increasing Mn content, as shown in figure 2.8. This demonstrates the dominance of exchange narrowing [38] over dipolar broadening [39]. Exchange narrowing is a quantum mechanical effect associated physically with a marked increase in the random motion of the spins in interacting magnetic (exchange-coupled) atoms [38]. Gesmundo and Rossi [40] concluded that Mn^{2+} ions can be exchange-coupled for distances at and smaller than the third nearest cation neighbors in MgO, corresponding to a distance less than 5.2 Å. In the 1:2 ordered hexagonal BZT lattice, a given Mn^{2+} in the B' site has 6 first nearest neighbors at a distance of 5.78 Å. The observation that exchange narrowing is very large for 6% Mn indicates that exchange-coupled Mn^{2+} clusters, rather than isolated Mn^{2+} ions, dominate the spectrum for this concentration and those above this value.

The observed magnetic field dependence of the loss tangent all the way to zero applied field for the 12% Mn-doped BZT sample at 50 K suggests that spin losses are significant in ambient magnetic fields and low temperatures.

2.4.2 Magnetic Field Dependence of Losses in Co-doped BZN

Figure 2.9 (a-e) shows that the Co^{2+} EPR resonance peak in BZN is at ~1410 G, corresponding to a gyromagnetic ratio in the range from 4.14 to 4.36. Also, similar high g values are found in other materials containing Co^{2+}, including single crystal MgO (g = 4.278) [41-43].

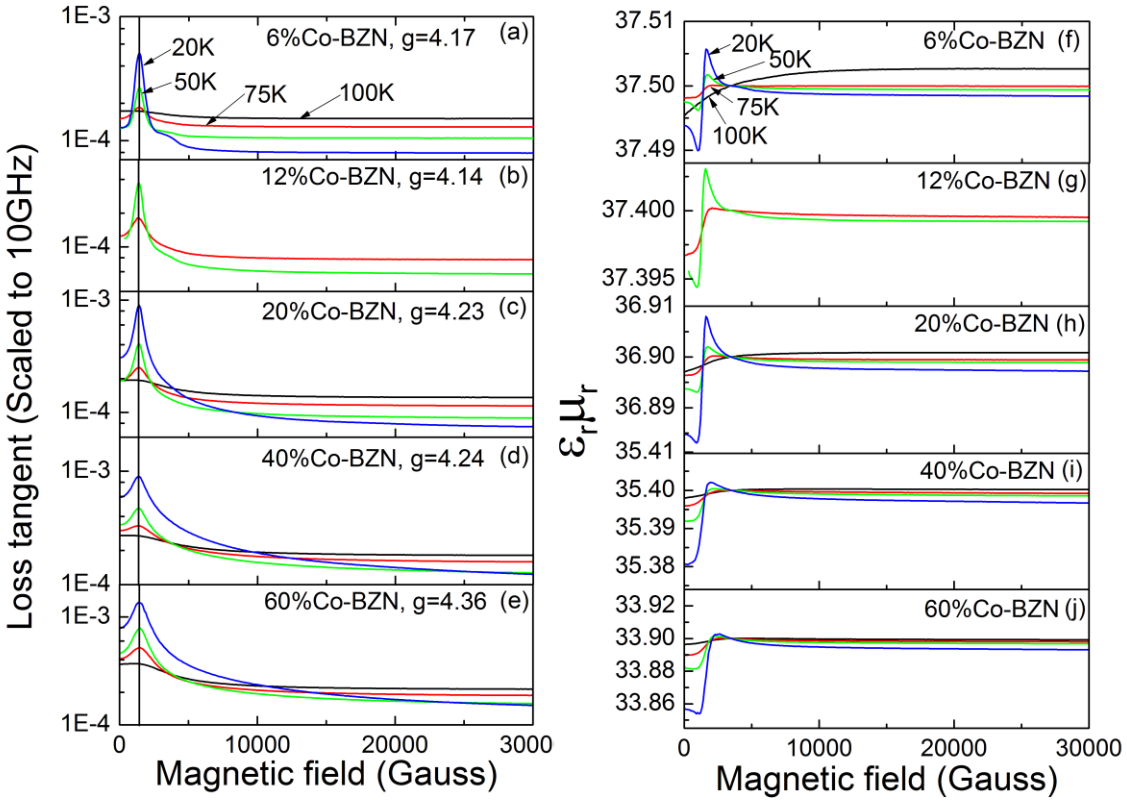

Figure 2. 9 Magnetic Field Dependence of Microwave Loss Tangent (a-e) and $\varepsilon_r\mu_r$ (f-j) of 6%, 12%, 12%, 20%, 40%, and 60% Co-doped BZT for Temperatures at 20 K (Blue-line), 50K (Green-line), 75K (Red-line), and 100 K (Black-line).

In Co-doped BZN samples, Co^{2+} ions are in an octahedral crystal field, which splits $3d^7$ ($^4F_{9/2}$) into 3 levels and the Kramers doublet ground state has symmetry T_{1g} [41-43]. The spin-lattice relaxation time for Co^{2+} in octahedral surrounding is very short because its lowest excited state is only 305 cm^{-1} above the ground state, and thus the Co^{2+} EPR resonance can only be observed at cryogenic temperature [43-44]. Although reference 41 observed the 8 hyperfine lines from the I=7/2 Co nucleus, none were resolved in our measurements of Co-doped BZN structure. Our measurements found a linewidth in the range of 450 to 800 Gauss, presumably as a result of broadening by the strong dipole-dipole interaction and internal strain [45].

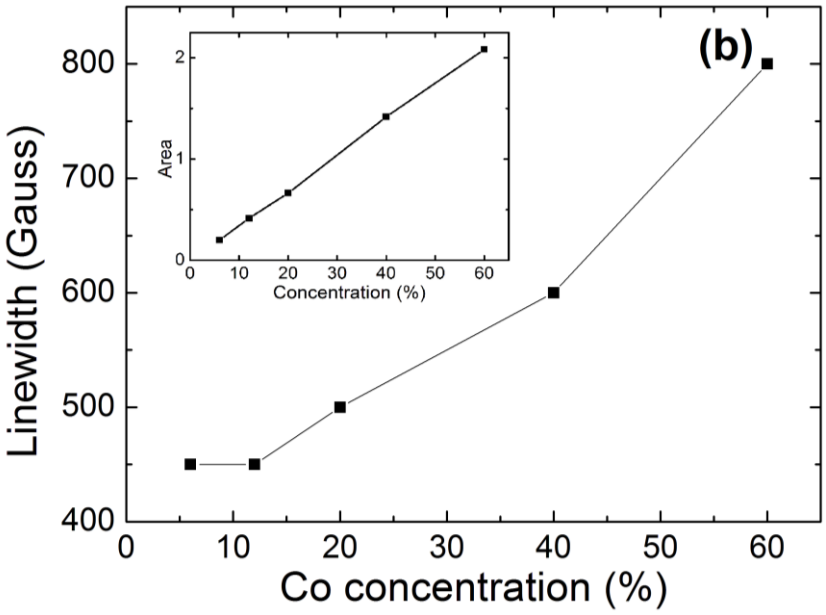

Figure 2. 10 Linewidth of The g = 4.17 Co^{2+} EPR Loss Tangent Peak (~1410 Gauss) at 50 K. The Linewidth is Determined By the $\Delta H_{Peak\text{-}Peak}$ of the First Derivative of Loss Tangent. Inset Shows the Integrated EPR Peak Area, Indicating That the Number of EPR Active Co^{2+} Increases Linearly With Alloying Concentration.

As shown in the inset of figure 2.10, the area under the Co^{2+} resonance peak, which is proportional to the number of EPR active Co^{2+} ions, is linearly related to the Co concentration. This result indicates that our dielectric-resonance EPR measurement configuration is able to measure all of the Co^{2+} ions in the sample. This is in contrast to some recent reports [44, 46] in which some of the Co^{2+} ions went undetected, and were labeled "hidden" pairs and clusters. We suggest that our direct measure of the high-Q of the resonator to detect EPR, without using derivative lock-in methods, is able to more readily discern broader and smaller EPR peaks. Temperature-dependent magnetic susceptibility measurements also find a linear dependence between the number of

magnetically-active Co^{2+} ions and the Co concentration for our samples, further validating our methods and conclusion that there are no "hidden" Co ions in our sample.

In a study of Co-doped MgO, Dyrek and Sojka [44] found that coupling was prevalent at similar molar concentrations. We note that the higher Co concentrations in BZN have predominantly only the dipolar broadened peaks associated with EPR from pairs and larger exchange coupled clusters. The width of the Co^{2+} peaks increase with increasing Co concentration as a result of dipolar broadening, shown in figure 2.10. Broadening is attributed to the fact that the number of nearest neighbors increases with the square of the distance and the interaction energy decreases with the inverse cube [47]. Exchange narrowing could affect the linewidth as well, but it is not a significant effect in these samples. It is noteworthy that the microwave loss mechanism in these samples has many similarities to our earlier findings on Ni-doped BZT [9].

In reference 44, the authors concluded that Co^{2+} ions in MgO are exchange coupled up to the third nearest cation neighbors, corresponding to a distance less than 5.2 Å. In the disordered pseudo-cubic BZN lattice, there are 6 B'B'' first nearest neighbor sites at a distance of 4.09 Å, and 12 next nearest neighbor sites at a distance of 5.78 Å. The similar broadening observed in the EPR measurements of the Co-doped BZT and BZN samples (i.e. magnetic-field dependence of the loss tangent) for the same Co-concentrations suggests that both the nearest neighbor and next nearest neighbor sites in BZN are involved in forming exchange coupled clusters in that material.

2.4.3 Temperature Dependence of Losses in Transition-Metal-doped BZT and BZN with and without External Magnetic Field

To better quantify this mechanism, figure 2.11 (a) shows the loss tangent of BZT with 12% Mn additives as a function of temperature in the absence of an applied field (ambient) and at 5 Tesla. Since the microwave photon energy is over an order of magnitude less than the Zeeman energy at 5 Tesla, EPR losses are insignificant under these conditions. Effectively the microwaves do not provide sufficient energy to undergo a spin flip process. Thus, the EPR spin excitation losses in ambient fields are equal to the difference between the curves in figure 2.11 (a) and are significant below 100 K and dominant below 50 K. The value of the loss tangent measured at the large field of 5 Tesla apparently have thus quenched the loss component from electron paramagnetic resonance. The peak observed in the loss tangent at ~100 K in some of the samples appears to be similar to that typically attributed to polaron conductions [5-7].

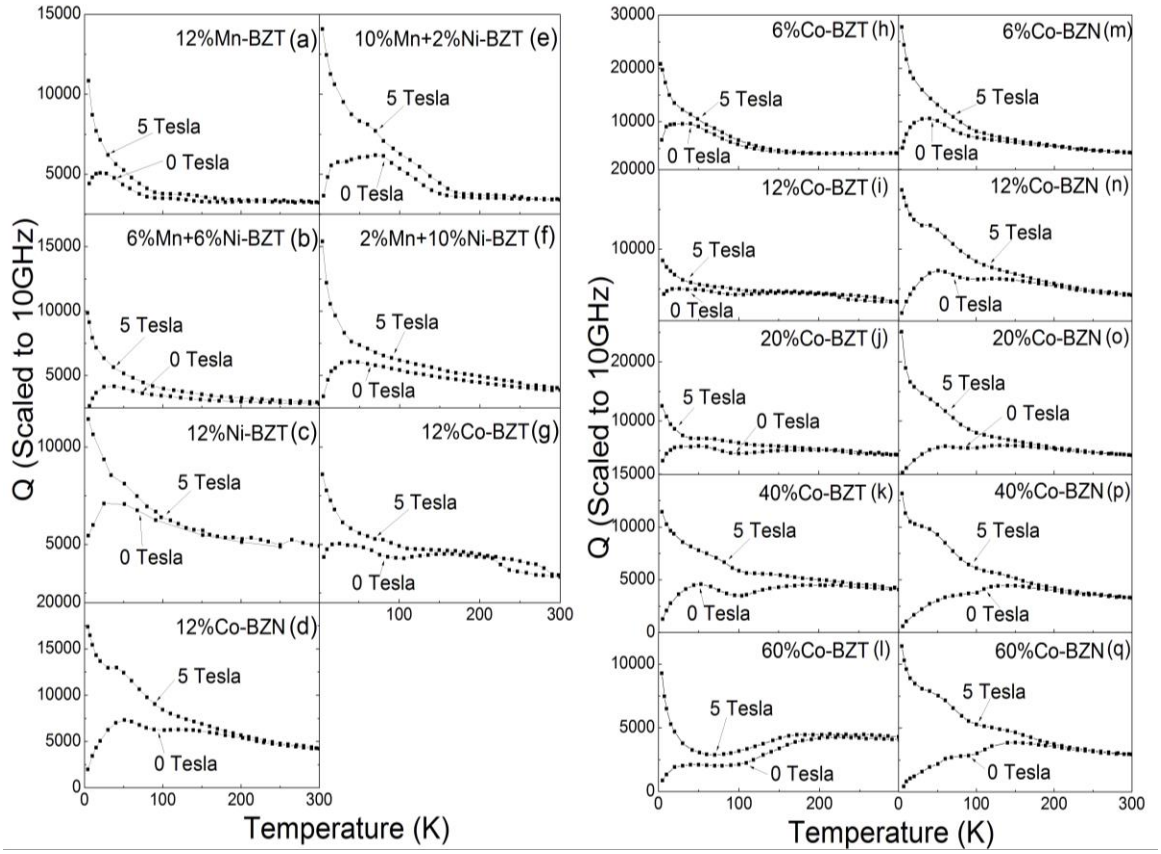

Figure 2. 11 Temperature Dependence of Loss Tangent at 0 Tesla (Upper Data and Line) and 5 Tesla (Lower Data and Line) for Co-doped BZT, Co-doped BZN, and Ni and Mn Doped BZT.

Figure 2.11 (a-g) compares the spin losses with other materials with the same total 12% B'-site magnetic impurity concentration (i.e. 0.8% mole fraction). It shows that Mn-doped material has the smallest spin losses in ambient field, then Ni, co-doped Ni-Mn and finally Co. Also, figure 2.11 (h-q) shows that the use of the host BZT for the same amount of Co additives results in comparably smaller spin losses in ambient field than BZN. The application of a 5 Tesla field results in a much higher increase in Q in BZN than BZT. We will focus much of the remaining discussions on Co-doped BZN.

Figure 2.11 shows that as temperature decreases, specifically below 150 K, the difference in loss between samples measured in ambient fields (zero applied magnetic field) and 5 Tesla becomes large. Our group reported that Ni and Mn-doped BZT 4.2 K could induce a marked decrease in the loss tangent using large magnetic fields [16]. Figure 2.11 (m-q) presents that Co-doped BZN at 5 Tesla exhibits much lower loss tangent than at zero applied field.

2.5 Kramers-Kronig Relation in EPR Losses

2.5.1 Introduction to Kramers-Kronig Relation

The Kramers-Kronig (KK) relation connects the real and imaginary parts of a complex system. We can calculate the real component from the entire spectrum of the imaginary part, or vise-versa using the KK relation. The KK relation only works if the system is causal. A causal system means the effect only occurs after the cause. For instance, a bell rings only after it is stricken, not before. Causality is met for this system because there is no resonant response until the microwave photon interacts with the Zeeman split electron spins.

Figure 2.12 (a) represents a single pulse signal coming into a system at time, t=0, where the system is only passing through a sine wave with certain frequency and amplitude, shown in figure 2.12 (b). Figure 2.12 (c) shows that when $t < 0$, before the arrival of the pulse signal, no absorption is occurred. When $t > 0$, the input pulse signal starts influencing the sine wave. We note that this is not a simple absorption process as the phase of the sine wave is also shifted over the whole time spectrum. Therefore, the

response must have both real and imaginary parts, because it describes the phase shifts at all the frequency to compensate the magnitude change caused by the absorption process.

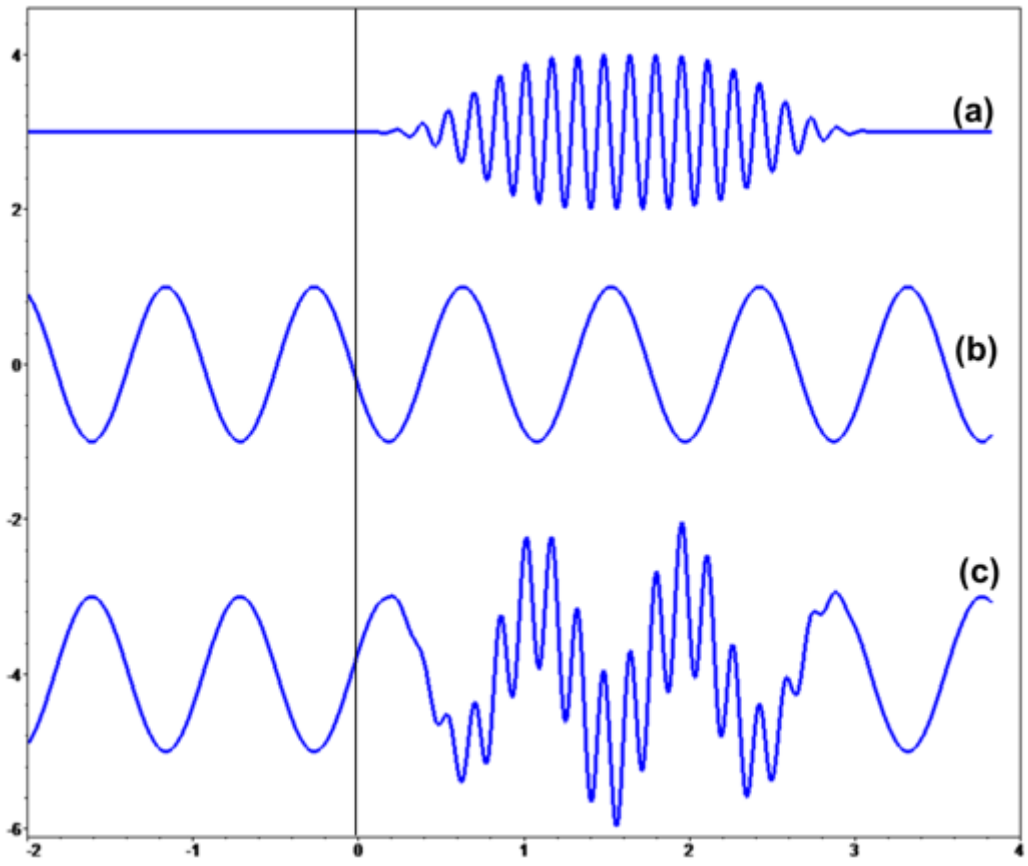

Figure 2. 12 A Representation of the Kramers-Kronig Relation; (a) Input: An Incident Pulse Signal; (b) A Sine Wave That Is Absorbed By the System; (c) The Response That Follows the KK Relation, A Causal System (Courtesy to Dr. Lei Yu).

2.5.2 The KK Relation between EPR Losses and Magnetic Reactive Response (μ_r)

The KK relation is expected to be applicable to our results as the magnetic field modifies the Zeeman energy to facilitate the resonance excitation by a microwave photon only after it arrives. This causality relation in conjunction with linearity (i.e. unsaturated

EPR peaks) satisfies the criteria required for application of the KK relations [48]. Figure 2.13 (a-b) shows that the loss tangent and $\varepsilon_r\mu_r$ of 0.75% Mn-doped BZT is accurately related by the KK relation (equations 2.5 and 2.6), where $\mu_r(B) = \mu_r'(B) - \mu_r''(B)$ and $\mu_r(B)$ is assumed constant and the loss tangent is defined as $\mu_r''(B)/\mu_r'(B)$.

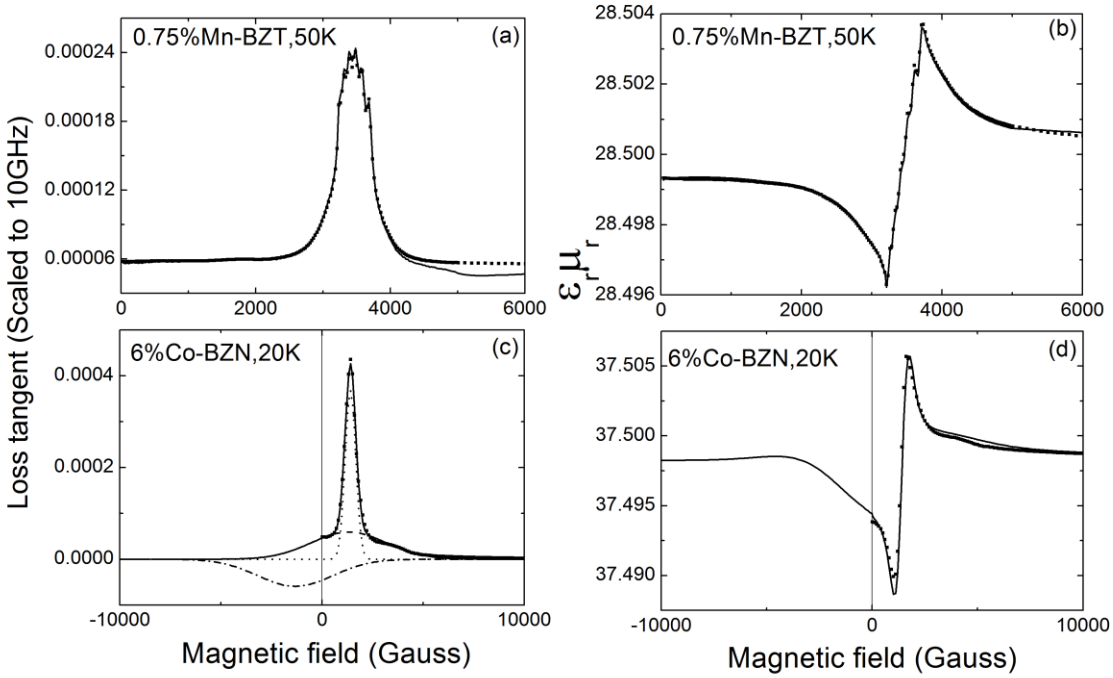

Figure 2. 13 (a) Loss Tangent Values of 0.75% Mn-BZT at 50 K Are Presented As Data Points and The Line is The Kramers-Kronig (KK) Transform (Equation 2.6) of the $\varepsilon_r\mu_r$ Values From the Same Sample (Shown in b). Note That the Fit is Remarkably Accurate. (b) $\varepsilon_r\mu_r$ of 0.75% Mn-BZT at 50 K Are Presented As Data Points and the Line Represents the KK Transform (Equation 2.5) of the Loss Tangent Values from the Same Sample (Shown in a). Note That the Fit Is Also Remarkably Accurate. (c) Loss Tangent Values of 6%Co-BZN at 20 K Are Presented As Data Points and the Solid Line is the Sum of Two Gaussian Peaks Fit to the Isolated Co^{2+} (Dot-line) and Exchange-coupled Pairs and/or Clusters (Dash-line). The Sum of These Two Components is Shown As A Solid Line. The Left-handed Signal Can Excite Co^{2+} Clusters in An Environment in Which the Net Field is in The Opposite Direction to the Applied Field. We Include This Peak As Well As A Dot-dash Line. This Occurs in Conditions in Which the Applied Magnetic Field Are Small Compared to Dipolar Broadening; (d) $\varepsilon_r\mu_r$ of 6%Co-BZN at 20 K Are Presented As Data Points and the Line Represents the KK Transform (Equation 2.7) of the Loss tangent Fit Using the Sum of All Three Components (Dot-line, Dash-line and

Dot-dash-line) Described Above From the Same Sample (Shown in c). Note That the Fit is Remarkably Accurate. The Solid Line in c is Given by the KK Transform (Equation 2.8) of the 3-line Fit in d, Indicating That Our KK Analysis Accurately Can Be Used to Relate the Real and Imaginary Parts of the Magnetic Permeability and Vice Versa.

$$\mu'(B) - 1 = -\frac{2}{\pi}\int_0^\infty \frac{B'\mu''(B')}{B'^2 - B^2}dB' \qquad \text{Equation (2.5)}$$

$$\mu''(B) = \frac{2B}{\pi}\int_0^\infty \frac{\mu'(B') - 1}{B'^2 - B^2}dB' \qquad \text{Equation (2.6)}$$

$$\mu'(B) - 1 = -\frac{1}{\pi}\int_{-\infty}^\infty \frac{\mu''(B')}{B'^2 - B^2}dB' \qquad \text{Equation (2.7)}$$

$$\mu''(B) = \frac{1}{\pi}\int_{-\infty}^\infty \frac{\mu'(B') - 1}{B'^2 - B^2}dB' \qquad \text{Equation (2.8)}$$

We found that the commonly-used KK methods are not appropriate when the dipolar broadened width is large compared to the applied externally applied magnetic fields. The reason is that an important component is not included in conventional EPR analysis which is needed here. Since a linearly polarized microwave source has both right hand and left hand circularly polarized components, the left handed polarization can excite resonance in the opposite direction from conventional EPR spin flips. When the dipole field is larger than the applied field, the local magnetic field is directed in the opposite direction from the applied field for a fraction of the Co^{2+} ions and a left-handed photon can cause a resonant spin flip is in the opposite direction to that of the traditional EPR excitation [49-50]. The EPR pioneers Abragam and Bleaney discussed this quantitatively in reference 49. This results in *μ'(B)* and *μ''(B)* no longer being even and odd, so the Kramers-Kronig equations 2.7 and 2.8 need to be used [51]. Thus, to carry out

the KK transform, two Gaussian peaks are used to fit the data. The first high narrow peak (dot-line) represents the EPR response from the isolated Co^{2+} ions, while a wide one (dash-line) represents the EPR response from the dipolar broadened clusters. A component of the wide dipolar broadened peak extrapolates to a finite contribution at negative fields, indicating that some of the Co^{2+} ions experience a net local field in the direction opposite to the applied field. These ions each contribute a negative moment to the susceptibility and can be excited by the left handed part of the microwave signal. To model this component, we include a negative susceptibility peak in the analysis, as shown in figure 2.13 (c). When both of the traditional EPR from the right hand circularly polarized component and the one from the left hand component are included in the calculation, equation 2.7 gives an impressive fit to the $\varepsilon_r\mu_r$ data in figure 2.13 (d).

2.6 Potential Practical Applications using EPR Losses

Figure 2.14 (a) shows that the Q of the $Ba(Co_{1/15}Zn_{4/15}Nb_{2/3})O_3$ composition (i.e. 20% doped Co in BZN) can be tuned over the range of ~1,100 to over 12,000 at liquid nitrogen temperatures (i.e. 77 K) through the application of magnetic fields easily reached by rare earth permanent magnets. This demonstrates that practical ultra-high Q passive microwave devices can be made with external control of their transfer function using magnetic fields.

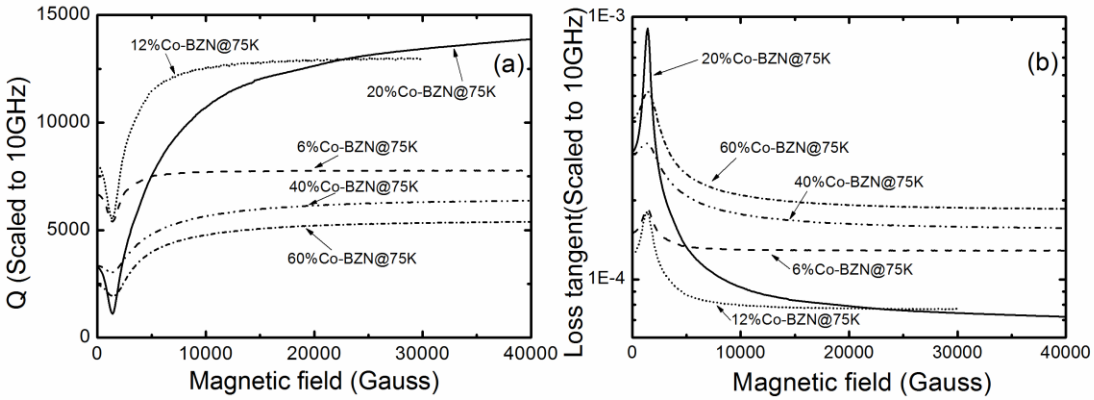

Figure 2. 14 (a) Q-factor Measurements of Co-alloyed BZN Over a Wide Range of Magnetic Fields Are Presented. The Corresponding Loss Tangent (=1/Q) is Shown in (b). Note that the Q of the 20% Co-BZN Can Be Tuned Over the Range of ~1,100 to Over 12,000 at Liquid Nitrogen Temperatures (i.e. 77 K) Through the Application of Magnetic Fields Easily Reached by Rare Earth Permanent Magnets. Also Note That the EPR Losses of Co^{2+} Clusters in This Sample Extend Up to Unusually High Fields, Approaching 40,000 G, Due to Dipolar Broadening of the Exchange-coupled Pairs and/or Clusters.

3. FUNDAMENTAL MECHANISMS THAT DETERMINE THE TEMPERATURE COEFFICIENT OF RESONANT FREQUENCY IN HIGH PERFORMANCE MICROWAVE DIELECTRICS

3.1 Introduction to Temperature Coefficient of Resonant Frequency (τ_f)

Advanced microwave filters require that the relative temperature dependence of the dielectric's resonant frequency, $\tau_f = (^1/_f)\ (^{df}/_{dT})$, be precisely set at zero or near-zero to achieve the required performance over a range of temperatures. A small non-zero τ_f is often chosen by system engineers to offset the small temperature dependence of the amplifiers.

Controlling τ_f to the desired value has been achieved empirically in low-loss materials by (a) doping, (b) alloying, and/or (c) combining multi-phase composite ceramic materials [4, 9, 52-56]. Surprisingly, at least to this author, almost all of the commercial microwave dielectric products on the market today tune τ_f through the addition of varying amounts of magnetic additives, such as Ni, Co, and Mn [4, 9, 52-56].

In this chapter, we study the microwave properties as a function of Ni content in $Ba([Zn_{1-x}Ni_x]_{1/3}Ta_{2/3})O_3$, a completely miscible solid solution whose microwave dielectric constant and τ_f vary smoothly and monotonically over the entire alloy series [56] shown in figure 3.1.

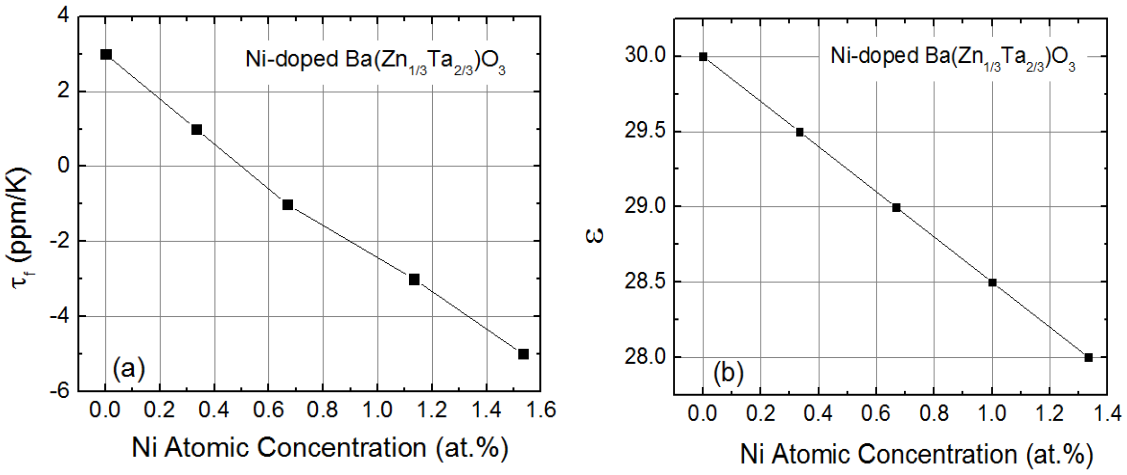

Figure 3. 1 τ_f (a) and ε (b) is Plotted As A Function of Ni Doping Concentration (at. %) in $Ba(Zn_{1/3}Ta_{2/3})O_3$ [56].

Despite the importance of τ_f for practical applications, a strong first-principles understanding of what determines this important parameter has not been established. In fact, only a handful of studies [57-60] have characterized the temperature-dependent parameters τ_ε, τ_μ, α_L, and/or τ_f of low-loss perovskite ceramics from cryogenic to room temperature. None have determined all of the parameters. Nor have they studied material with a near–zero temperature-compensation at room temperature. Gvasaliya et al [58] studied $Ba(Mg_{1/3}Ta_{2/3})O3$ ($\tau_{f\,@300\,K}$ = 5.4 ppm/K) and found that the degree of Mg^{2+}/Ta^{5+} does not significantly influence the material's thermal expansion. Neutron scattering was used to measure the thermal expansion of $BaZrO_3$ ($\tau_{f\ @300\ K}$ =~140 ppm/K) at three different temperatures between 2 to 300 K [59-60], making it difficult to observe systematic trends.

In our study, we have experimentally measured α_L, τ_f, and τ_μ of BZT, Ni-doped BZT and BNT, allowing us to determine τ_ε over the temperature range of 2 to 300 K. We also performed first-principles simulations of the electronic and phonon structures of the

compounds. This has allowed us to gain a fundamental quantitative understanding of the mechanisms responsible for the observed temperature dependence of these parameters. We will show that at low temperatures, the paramagnetic response dominates τ_f in materials containing "magnetic" doping and alloying. At higher temperatures, we will show that the addition of these elements also affects the electronic and phononic structure, allowing controllable tuning of this important parameter.

3.2 Determination of Temperature Coefficient of Resonant Frequency (τ_f) in Dielectric Resonators

In this chapter, the resonant frequencies were determined using microwave dielectric resonator (DR) measurements discussed in chapter 2. The resonant frequencies of the rectangular DRs were measured at the $TE_{11\delta}$ mode in the range of 9.5–10.0 GHz for the samples in this study. Static dielectric constants, ε_0, were measured by a conventional $TE_{01\delta}$ measurements technique, on a 2.6 to 2.8 cm diameter, ~0.5 cm thick puck samples in an 8.0 cm diameter x 7.0 high cylindrical gold-plated copper cavity at room temperature [26].

In figure 3.2, we first present experimental determinations of τ_f for BZT, BNT, and 0.8 at. % Ni-doped BZT, the factor of interest to microwave system designers. At room temperature, all three dielectrics of interest have τ_f of less than 20 ppm/K. As the temperature drops, the τ_f reduces gradually in magnitude and reaches a minimum at ~50 K. When the temperature cools down further, τ_f starts to increase. The τ_f of BZT returns to near-zero again, and the τ_f of 12% Co-BZT is slightly larger than that of BZT at 4 K.

The τ_f of 12% Ni-BZT increases significantly at lower temperatures and approaches ~30 ppm/K at 4 K. At cryogenic temperatures, BNT exhibits significantly larger τ_f than the rest, increasing to as high as ~110 ppm/K. Then, in the remainder of the section, we give experimental and simulation results for α_L, τ_ε, and τ_μ parameters that describe the temperature dependence of the physical properties that determine this important factor.

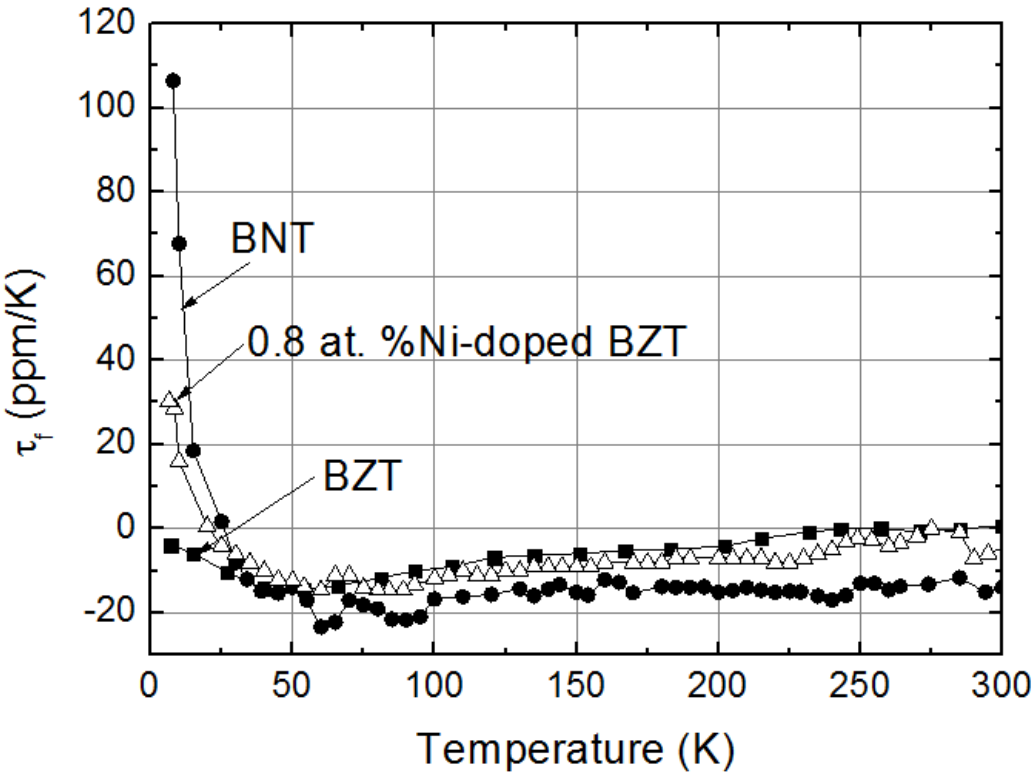

Figure 3. 2 Temperature Coefficient of Resonant Frequency (τ_f) of the BZT, 0.8 at. % Ni-doped BZT, and BNT.

3.3 Characterization and Simulation of Thermal Expansion (α_L) in Dielectric Materials

Thermal expansion (α_L) measurements were performed using the recently-developed dilatometer option for the Quantum Design PPMS. The fused silica dilatometer cell uses a differential capacitive technique to measure thermal expansion and magnetostriction of samples.

We provide experimental determinations of the 2nd temperature-dependent factor, α_L, and show that it can be quantitatively modeled and understood using our density functional technique (DFT) calculations. In figure 3.3 (a), we see that our thermal expansion data for BZT, 0.8 at.% Ni-doped BZT, and BNT up to ~200 K can be accurately fit to the Debye equation for the specific heat and Grüneisen analysis [5] with a characteristic Debye temperature of 392 K, 392 K, and 408 K, respectively. When the temperature is above 200 K, α_L starts to deviate from the Debye model as a result of the extra weight of softened modes near the Brillion zone boundaries due to an antidistortive transition, as shown in the phonon simulations in figure 3.4. It is also noticed that the thermal expansion reduces as the amount of transition-metal components increases, which is often correlated to the smaller atomic weight and shorter effective ionic radii of Ni^{2+} than Zn^{2+} [61].

In the inset of figure 3.3 (a), we notice a peak in the thermal expansion of BNT at 3.3 K which is the characteristic of the transition from the antiferromagnetic state at low temperature to the paramagnetic state at higher temperature [62]. DFT calculations find that the ground-state antiferromagnetic at 0 K exists in an intralayer-ferromagnetic and

interlayer-antiferromagnetic structure. A peak in the BNT magnetic permeability at 3.3 K (inset of figure 3.6 (b)) confirms this.

Figure 3.3 (b) shows the linear lattice expansion (ΔL/L) of BZT and BNT, which is calculated by the integration of the experimental α_L shown in figure 3.3 (a). We see that the lattice expands ~0.2 % from 2 K to 300 K for both BZT and BNT.

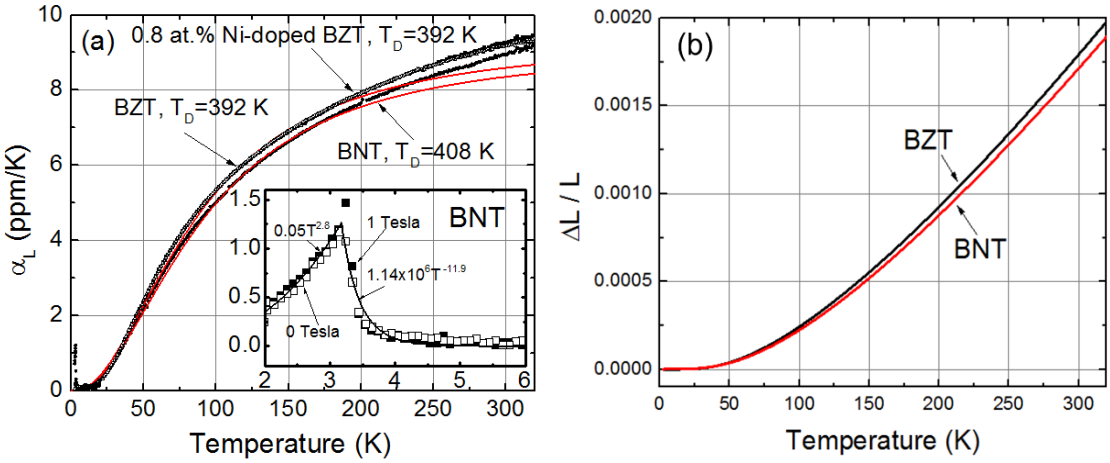

Figure 3. 3 (a) Thermal Expansion (α_L) Measurement Values for BZT, 0.8 at.% Ni-doped BZT, and BNT Are Represented As Black Data Points and the Debye Equation Fits Are Shown As Red Solid Lines. The Inset Shows BNT's Neel Temperature at 3.3 K, Characteristic of A Phase Transition from the Antiferromagnetic State at Low Temperatures to the Paramagnetic State. From 2 K to 3.3 K, the Data is the Best Fit With A $0.05T^{2.8}$ Relation, and From 3.3 K to 6 K the Best Fit is $1.14T^{-11.9}$. (b) Temperature Dependence of Lattice Expansion of BZT (Black-line) and BNT (Red-line), as Derived from the Integration of the Experimental α_L. At 300 K, the Lattice Expansions of BZT and BNT are Similar and ~0.002 (0.2%).

To simulate the lattice dynamics, the phonon frequency ($\omega = E/\hbar$) versus wave vector (k) curves are simulated shown in figure 3.4. From the slope of the lowest energy acoustic phonon mode, we estimate the Debye temperature of BZT and BNT to be 444 K and 483 K respectively at the zero-temperature equilibrium lattice constant, and 433 K

and 476 K at the experimentally-determined 300 K lattice constant, which are ~15% higher than found when fitting experimental data. This is a reasonable agreement, given that our estimate of the Debye temperature from the theory comes only from the lowest energy acoustic mode. Both theory and experiment find that BNT has a larger Debye temperature than BZT.

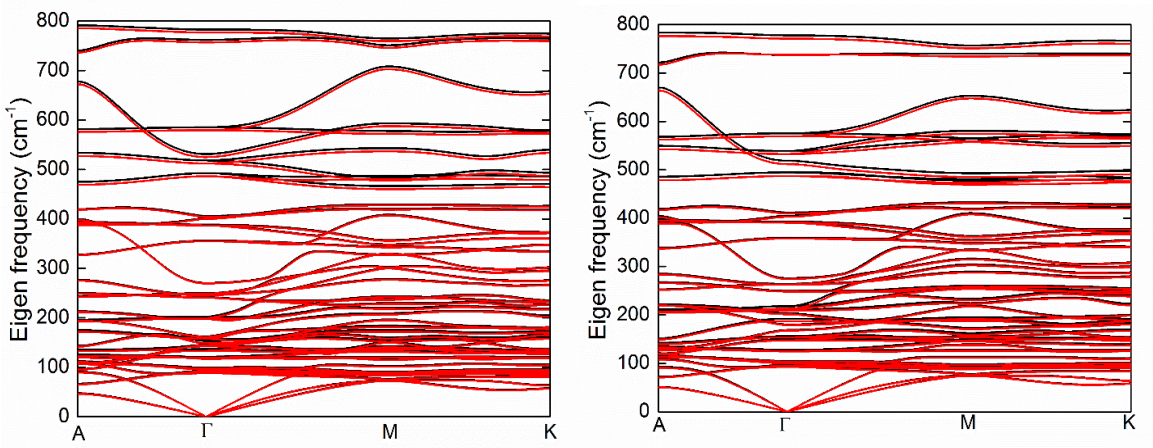

Figure 3. 4 Phonon Eigen Frequency (ω = E/ħ) vs. Wave Vector (k) Curves of BZT (Left) and BNT (Right) with Relaxed Lattice at Equilibrium and at 0 K (Black Lines) and at a 0.2% Lattice Enlargement (Red Lines), the Experimentally-measured Increase at ~300 K (Figure 3.3 b). The 0.2% Expanded Lattice is Used to Simulate the Properties at 300 K. This is Based on the Concept that a Solid's Properties Can Be by Adequately Modeled by Considering the Lattice Softening Alone Upon Lattice Expansion, As Has Been Generally Accepted by the Field [63].

We can infer α_L from the DFT calculations of the heat capacity (C_v) using $\alpha = \gamma C_v / 3B$ (Figure 3.5), where γ is the average Grüneisen parameters and B is the bulk modulus [5]. γ is deduced from equation 3.1,

$$\gamma = -\frac{\partial(\ln\omega)}{\partial(\ln V)} \qquad \text{Equation (3.1)}$$

where ω is the average Debye frequency of average acoustic modes, V is the unit cell volume [5]. The Grüneisen parameter of BZT and BNT are calculated to be 2.39 and 1.66, respectively.

Determinations of B_{BZT} = 209 GPa and B_{BNT} = 152 GPa were inferred by scaling the theory relation to the experiment values in Figure 3.5. We note that the theoretical results closely follow the measurement values, particularly below 50 K and above 175 K. These observations again confirm that the theoretical calculations can adequately model the phonon dynamics in these materials.

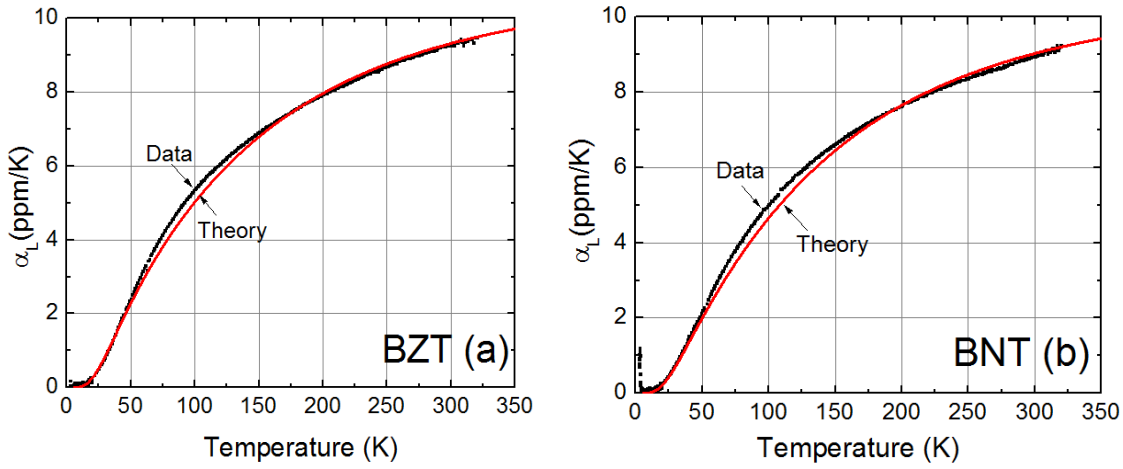

Figure 3. 5 Thermal Expansion Measurements (Black Data Points) and DFT Calculations (Red Solid Lines) of BZT (a) and BNT (b) with 2 % of Lattice Expansion.

We also used the theory alone to model the bulk modulus of BZT and BNT. We changed the volume of the unit cell from -2% to 2% with step of 1% and obtained the energy (E) as a function of volume (V). Then, a second order polynomial function was used to fit the E vs. V data, and the bulk moduli of BZT and BNT were calculated by

taking the second order derivative of E with respect to the V, as shown in equation 3.2. Our calculations show that the bulk moduli of BZT and BNT are 138.10 and 138.75 GPa, respectively.

$$B = V\frac{d^2E}{d^2V}$$ Equation (3.2)

3.4 Measurements and Simulation of Temperature Dependence of Magnetic Permeability (τ_μ) in Dielectric Materials

Next we show the temperature dependence of permeability (μ) and its temperature-derivative, τ_μ, in Figure 3.6. Magnetic susceptibility determinations were performed using a VSM option for the Quantum Design PPMS system (Model 6000; Quantum Design, San Diego, CA). The magnetic permeability (μ) is determined by using equation, $\mu=1+{}^{M}/_{H}$, where M is the magnetization and H is the applied magnetic field.

We measured the temperature dependence of magnetic permeability on BZT, BNT, and 0.8 at. % Ni-BZT. Results are shown in figure 3.6 (b). For BZT, we only measured negative susceptibility over the whole temperature range because of its diamagnetic characteristics. Note that the μ of BNT follows the expected Curie-Weiss law, Constant/T - Θ, and τ_μ follows it's derivative, - Constant/$(T - \Theta)^2$ from 3.3 K to 300 K, with a Weiss temperature (Θ) of - 8.37 K [5]. When the temperature is below the Neel temperature, 3.3 K, the BNT transitioned to antiferromagnetic phase, which shows a discontinuity in both μ and τ_μ. The μ and τ_μ of 0.8 at.% of Ni-doped BZT can also be accurately fit with the Curie-Weiss law with a Weiss temperature of - 1.12 K, as shown in

figure 3.6 (b). The paramagnetic center's effective magnetic moment (μ_e) is inferred from the Curie constant obtained from the Curie-Weiss law fit. The μ_e of BNT and 0.8 at. % Ni-doped BZT are 2.87 and 2.98, respectively. These values are slightly larger than the spin-only values (2.83 for Ni), because the orbital moments of Ni^{2+} are not completely quenched [5].

Figure 3.6 (a) shows that the influence of the magnetic permeability (τ_μ) on τ_f is essentially insignificant from 300 K to 20 K as the magnitude is less than 2 ppm/K. As the temperature is lower than 20 K, the τ_μ of 0.8 at. % Ni-BZT reduce to more negative values and approach to ~ -13 ppm/K at 2 K. For BNT, its τ_μ decreases to ~ -10 ppm/K at 3.3 K, but change abruptly to ~15 ppm/K as the temperature is reduced to antiferromagnetic phase.

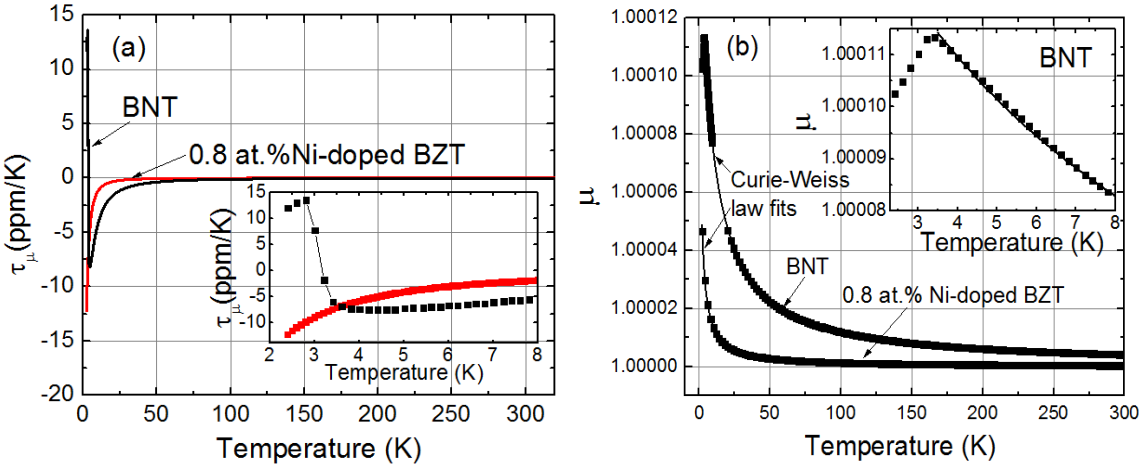

Figure 3. 6 (a) Temperature Coefficient of Magnetic Permeability (τ_μ,) of BNT and 0.8 at.% Ni-doped BZT Characterized using VSM (PPMS, Quantum Design) at 40 Hz. The Inset Shows the τ_μ from 2 to 8 K; (b) Temperature Dependence of Permeability (μ) of BNT and 0.8 at.% Ni-doped BZT, and Black Solid Lines Are the Curie-Weiss Law Fits. The Inset Shows the Antiferromagnetic Neel Temperature of BNT is 3.3 K.

3.5 Determination of Temperature Coefficient of Dielectric Constant (τ_ε) in Dielectric Materials

To obtain the last unknown parameter, the temperature dependence of dielectric constant (τ_ε) can be inferred from equation $\tau_\varepsilon = -(2\,\tau_f + 2\,\alpha_L + \tau_\mu)$ shown in figure 3.7. The results show that BZT and 0.8 at. % Ni-BZT have slightly negative τ_ε at and near room temperature, while BNT is positive. As the temperature decreases, their τ_ε all increase and reach a maximum positive τ_ε at ~40 K and then decrease at lower temperatures. We note that as the Ni concentration increases, the τ_ε experiences a sharper decrease to negative values at cryogenic temperatures.

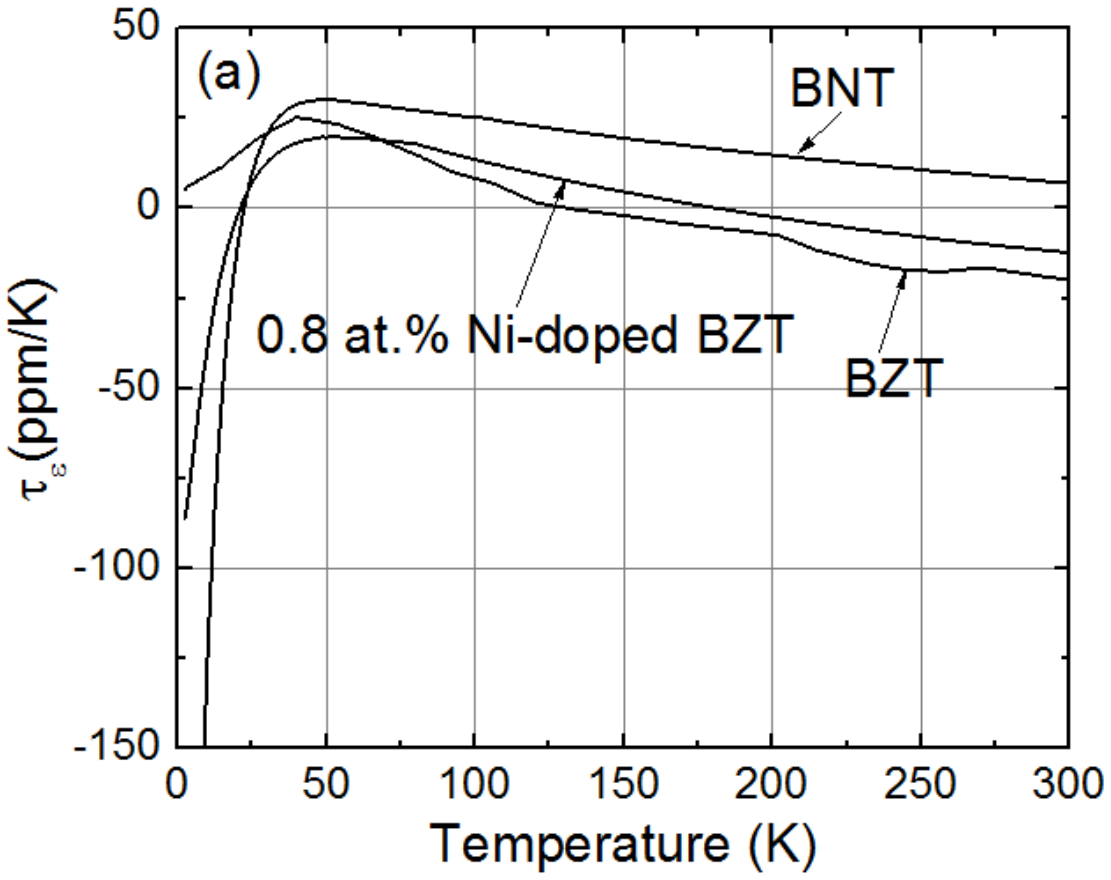

Figure 3. 7 Temperature Coefficient of Dielectric Constant (τ_ε) for BZT, 0.8 at.% of Ni-doped BZT, and BNT is Inferred By the τ_f, α_L, and τ_μ.

We calculate the dielectric constants (ε) as a function of temperature by integrating the τ_ε (figure 3.7) and then multiplying the normalized dielectric constants with the static dielectric constant, ε_0 [26], as shown in figure 3.8. We notice that for BZT and 0.8 at.% of Ni-doped BZT, the dielectric constant increases when the temperature reduces from 300 K to 150 K, and start decreasing when the temperature cools down further. However, the ε of 0.8 at.% of Ni-doped BZT start increasing again when the temperature further decreases from 20 K to 2 K. The changes in ε of BZT and 0.8 at.% Ni-doped BZT (at ~10 GHz) between 300 K and 2 K are ~0.010 and ~0.008, respectively.

The ε of BNT drops almost linearly from 300 K to 25 K, but starts to increase as the temperature reduces below 20 K. At 20 K or lower, we note that the ε increases as the transition-metal concentration increases. Figure 3.8 shows that the ε of BNT is decreased by ~0.06 from 300 K to 2 K.

The red solid lines in figure 3.8 show that from 2 K to 20 K, the magnitude of ε of 0.8 at.% Ni-BZT and BNT roughly scales with the Ni content and can be reasonably fit with a Curie dependence with equation of $(^{Constant}/_{T})+ \varepsilon_{\infty}$, a relation that is found when paraelectric defects are present in a wide range of other materials [63-66]. This must result from reorientation over an energy barrier of (a) an asymmetric Ni atom in the lattice, (b) a spectator defect around the Ni or (c) a d-shell electronic state. This is a surprising result and warrants further study.

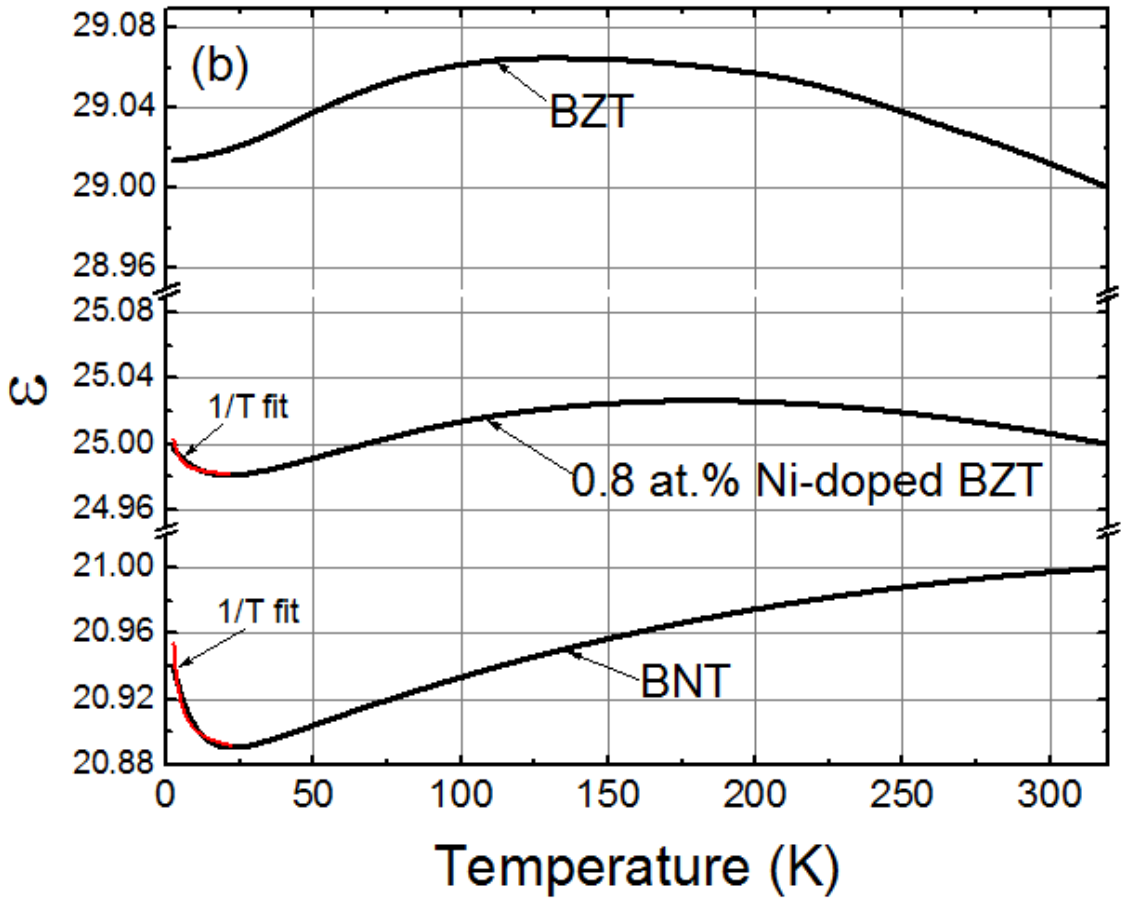

Figure 3. 8 Temperature Dependence of Dielectric Constant (ε) is Obtained by Integrating the τ_ε and then Multiplying the Normalized Dielectric Constants with the ε_0 of 29, 21, and 25 for BZT, 0.8 at.% Ni-BZT, and BNT, Respectively. The Red Solid Lines are the Curie Fits Which Show Reasonable Agreement at Low Temperatures.

3.6 Temperature Dependence of Dielectric Constant from Electronic Contribution

We will now show why the temperature dependence of dielectric constant in BNT is different from the pure BZT compound, and how Ni influences the phonon spectrum and its associated dielectric constant shift with temperatures.

DFT calculations in figure 3.9 shows the electronic contribution to ε of BZT and BNT between zero and 0.2% lattice expansion, from 0 eV (0 Hz) to 10 eV, equivalent of 2418 THz. The ε of BZT and BNT at 10 GHz (~40 μeV) are increased by ~0.007 (from

3.051 to 3.058) and ~0.018 (from 3.667 to 3.685), respectively. Thus, the changes in the electronic polarizability accounts for ~70 % (~0.01) and ~30 % (~0.06) of the shift associated with ε of BZT and BNT over this range.

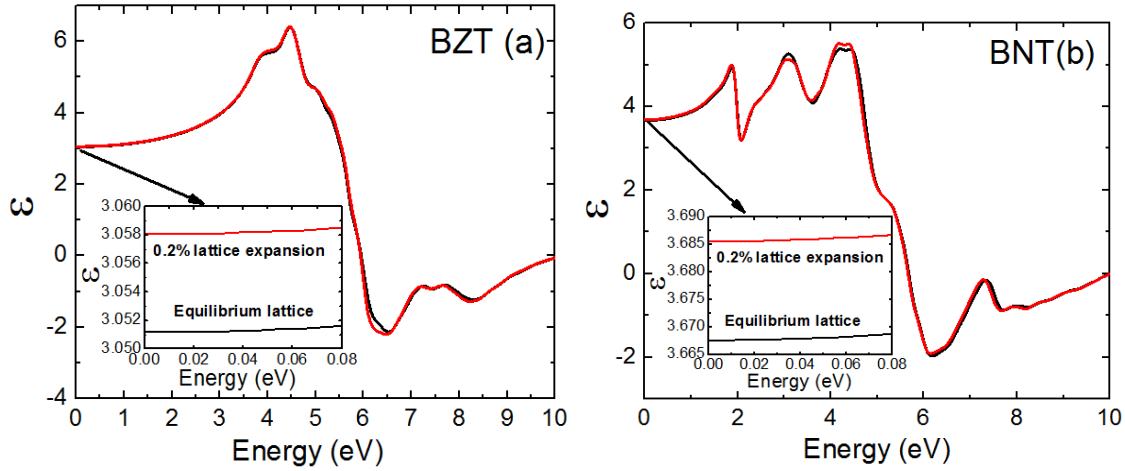

Figure 3. 9 The Electronic Contribution to the Dielectric Constant of BZT (a) and BNT (b) with Equilibrium Lattice Spacing and 0.2 % of Lattice Expansion from DFT Calculations.

3.7 Temperature Dependence of Dielectric Constant from Phonon Contribution

Now we discuss the phonon contribution to τ_{ε}. Dai et al. [67-68] shows that the matrix elements of the lattice dielectric constant of BNT are 20.74 and 16.65 for $\varepsilon_{ph,\,11}$ and $\varepsilon_{ph,\,33}$, respectively, which are determined by the doubly generated E_u mode and singlet A_{2u} modes.

We performed Raman spectroscopy measurements on BZT and BNT at 77 K and 295 K in figure 3.10. Table 3.1 summarized the measured A_{1g} and E_g modes at 77 K and 295 K, respectively.

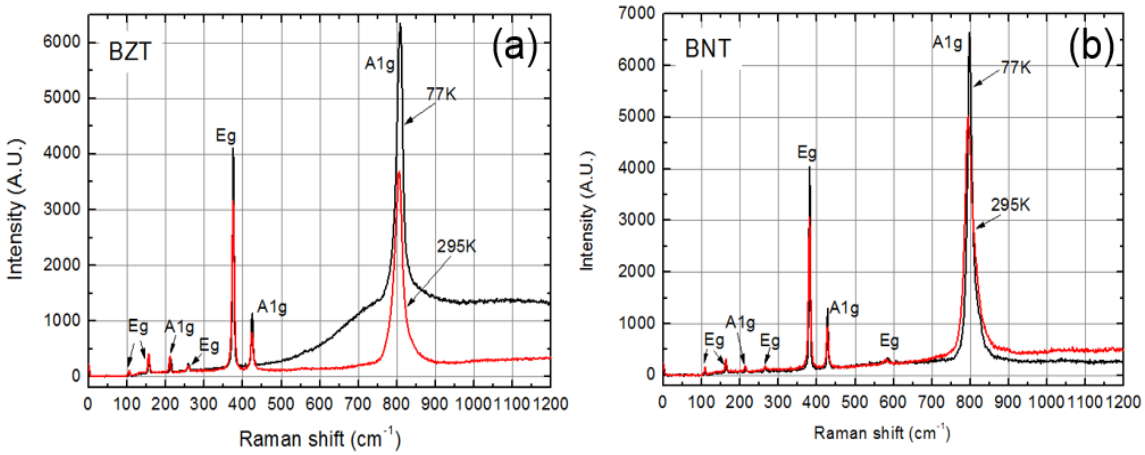

Figure 3. 10 Raman Spectroscopy Measurements of BZT and BNT at 295 K and 77 K.

Table 3. 1 Summary of the Raman-active Modes Wavenumber (cm^{-1}) of BZT and BNT at 77 K and 295 K Measurd by Raman Spectroscopy.

Raman Modes of BZT	Mode Position of BZT at 77 K (cm^{-1})	Peak Position of BZT at 295 K (cm^{-1})	Raman mode shift (cm^{-1})	Mode Position of BNT at 77 K (cm^{-1})	Peak Position of BNT at 295 K (cm^{-1})	Raman Mode Shift (cm^{-1})
A_{1g}	807.5	804.5	3.0	798.6	796.8	1.8
E_g	Not seen	Not seen	Not seen	585.1	580.9	4.2
A_{1g}	424.0	423.6	0.4	427.9	427.4	0.5
E_g	375.2	374.9	0.3	380.9	380.8	0.1
E_g	258.8	258.3	0.5	265.7	265.7	0
A_{1g}	213.2	210.2	3.0	215.2	213.2	2.0

E_g	156.5	155.6	0.9	163.8	162.8	1.0
E_g	105.7	105.1	0.6	105.7	105.1	0.6

We anticipate that our work will encourage theoreticians to use DFT calculations to model the temperature dependence of the dielectric constant. Dai et al [67-68] reported a method to calculate the zero-temperature dielectric constant using the phonon modes and the oscillator strengths inferred from DFT calculations. Since a solid's temperature-dependent phonon-related properties can be adequately modeled by only considering the lattice softening upon lattice expansion [63], DFT calculations of the changes in the phonon spectra at Γ as a function of lattice spacing, combined with our temperature-dependent lattice expansion measurements, can be used to predict τ_ε.

4. IN-SITU ELECTRON PARAMAGNETIC RESONANCE OF PERFORMANCE-DEGRADING DEFECTS IN SUPERCONDUCTING MICROWAVE RESONATORS

4.1 Introduction

Planar microwave devices, such as stripline, microstrip, and coplanar structures, are utilized to fabricate microwave resonators, filters, tuned amplifiers, and oscillators. The performance of these devices is limited by dielectric and metal losses [14-18]. At sufficiently low temperature, metal losses in these devices can be reduced by several orders of magnitude using superconducting electrodes [17-18]. A broad range of applications have employed superconducting microwave resonators due to their extremely low loss, such as kinetic inductance detectors (KID) [19-20], quantum memory [21-23], superconductor logic circuits [24], and quantum circuits [25].

Although the fundamental dielectric loss mechanism responsible for microwave loss in practical dielectrics is not fully understood, it is well accepted that intrinsic loss arises from multiple anharmonic phonon processes [10-11]. However, as we discussed earlier, at low temperatures, the losses in some high-performance commercial microwave dielectrics are dominated by EPR loss in exchange-coupled transition-metal clusters [4, 9, 26]. Furthermore, losses in many dielectric materials at ultra-low temperature and low microwave power levels, are dominated by two-level systems (TLS) [69-70] that can arise from low-energy atomic motion [71]. From these facts, we can conclude there is much to be learned by determining the nature and concentration of the defects that affect the performance of microwave resonators.

In this chapter, I first discussed the design, simulation, fabrication, and testing of superconducting parallel plate and u-shape stripline resonators. By employing these two types of superconducting microwave resonators, I developed an *in-situ* EPR spectroscopy, and the technique was validated by measuring the Q-factors as a function of magnetic fields applied parallel to the superconductor electrode surfaces with dielectrics that contain known transition-metal dopants (i.e. Co and Mn). Lastly, I used this novel technique to identify and quantify the performance degrading paramagnetic defects in conventional high purity semiconductors.

4.2 Design, Simulation, Fabrication, and Testing of Superconducting Microwave Resonators

4.2.1 Parallel Plate Resonators (PPR)

4.2.1.1 Design and Simulation of PPR

A superconducting PPR technique is composed of two superconductor thin-films "sandwiching" a thin piece of dielectric spacer in between. This technique has been extensively used to measure the surface resistance of superconductor thin-films due to various advantages. Firstly, the superconducting ground planes have very small low surface resistance (R_s) and high fill-factor, so it offers high Q-factors and sensitivity. Secondly, the movable coaxial cables can adjust the coupling *in-situ*, so the unloaded Q-factors of a PPR resonator can be determined readily. Thirdly, this technique eliminates the need for patterning or other sample preparation. Lastly, it also has well defined and understood resonant modes.

HFSS simulation is performed to investigate the resonant frequencies, electric and magnetic field patterns of each mode. In a 3D structure, a 10 mm x 10 mm x 0.5 mm Si substrate (ε_r = 11.9) is placed in the Cu cavity that is discussed in the previous chapter. Two 10 mm x 10 mm perfect conducting (PEC) square patches are placed in the model on the top and bottom surfaces of the Si substrate, serving as superconducting ground planes.

The resonance solutions (f = resonant frequency) for a rectangular PPR resonator with open-circuit boundary conditions can be written as [34],

$$f^2 = \frac{c^2}{\varepsilon_r}\left[\left(\frac{n}{2L}\right)^2 + \left(\frac{m}{2W}\right)^2\right] \qquad \text{Equation (4.1)}$$

where c is the speed of light, 3 x 10^8 m/s, ε_r is the realtive dielectric constant of the middle dielectric layer, n and m are mode indices, and L and W are the x- and y- length of the rectangular resonator, which are both equal to 10 mm in this thesis.

The fundamental modes (n=1 and m=0 or n=0 and m=1) for Si dielectric layer are calculated to be at ~4.35 GHz using equation 4.1.

Figure 4.1 shows that the S_{21} of the PPR resonator as a function of frequency simulated using the Driven Modal option in the HFSS software. We observed a series of transverse electromagnetic (TEM) mode resonant peaks. These are labeled this way because there are neither electric nor magnetic fields propagating in the longitudinal direction.

The fundamental modes $TEM_{10/01}$ are found at ~4.5 GHz in the simulation, which is consistent with equation 4.1. There would be expected to be a small, but significant difference given that the boundary conditions are not pure open-circuit at the metallic

surfaces of the Cu cavity and end plates. The small splitting of the degeneracy of the fundament modes in the simulation results from the slight coupling difference in the x- and y- directions. This effect, along with the sample not being perfectly square, explains why this is also experimentally observed in the PPR measurement.

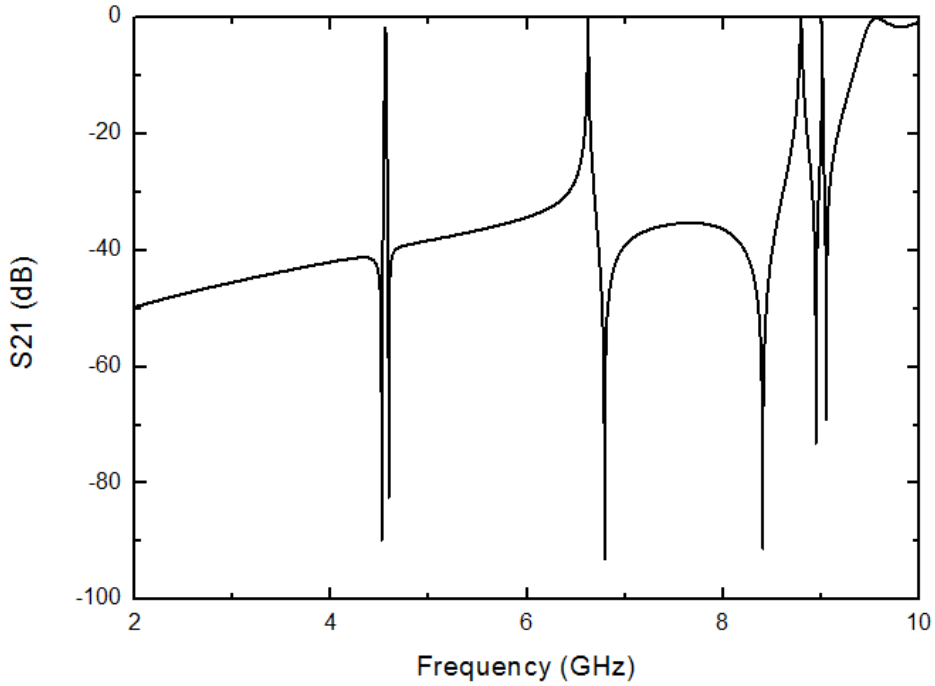

Figure 4. 1 HFSS Simulation of S_{21} vs Frequency from 2 to 10 GHz for PPR Resonator Using Si (ε_r = 11.9) as the Dielectric Layer and Perfect Conductors (PEC) as the Ground Planes in the Cu Cavity.

The electric fields of the first resonant peak at 4.54 GHz are plotted in magnitude and vector form in figure 4.2. The red and blue color lines represent the highest and lowest electric fields, respectively. The maximum fields appear at the edges, and minima field appears in the middle, characteristic of a half wavelength mode. This is confirmed by the contour of the electric fields in the vector form in the transverse plane shown in figure 4.2.

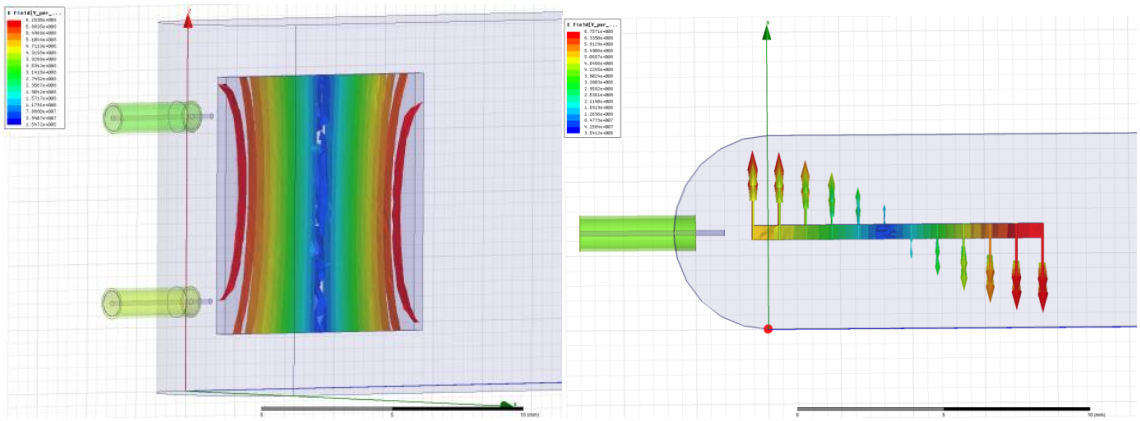

Figure 4. 2 Electric Fields of the First Resonant Mode at 4.54 GHz in the Form of Magnitude and Vector.

The second mode (TEM $_{m=1 \text{ and } n=1}$) is calculated using equation 4.1 to resonate at ~6.2 GHz, and the simulation finds it at ~6.65 GHz. Figure 4.3 shows half-wavelength wave patterns in both the x- and y- direction, so the second order mode is the weighted sum of two degenerate modes, TEM_{10} and TEM_{01}. The third set of resonant peaks, TEM_{20} and TEM_{02} modes, are observed at ~9 GHz in figure 4.1, whose electric fields should exhibit a full-wavelength pattern in both the x- and y- direction.

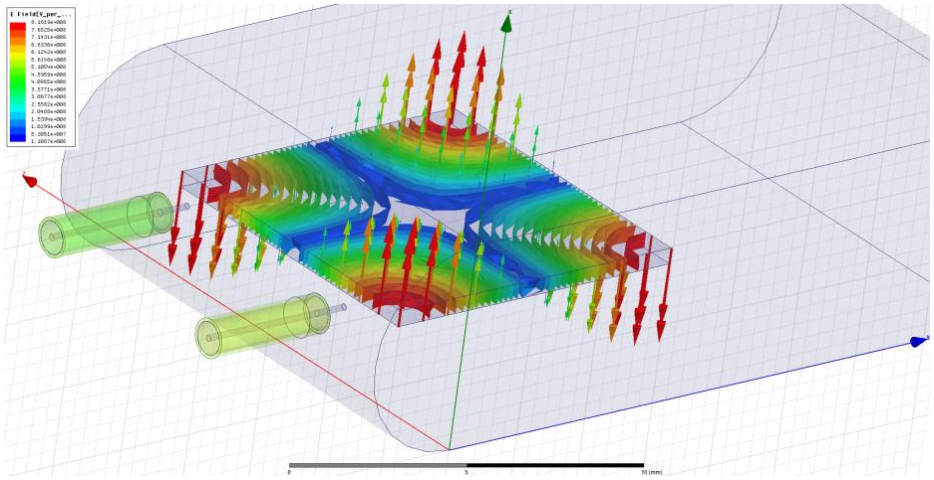

Figure 4. 3 Electric Field of the Second Order Mode (TEM_{11} mode) of a PPR Resonator at 6.65 GHz.

In this chapter, most of the *in-situ* EPR measurements with the PPR technique use the first or second order modes ($TEM_{10/01}$ and/or TEM_{11}).

4.2.1.2 PPR Fabrication

The superconducting electrodes of interest in this thesis are niobium (Nb), $YBa_2Cu_3O_{7-\delta}$ (YBCO), and magnesium diboride (MgB_2). The Nb (~300 nm thick) superconducting thin film electrodes have been deposited using planar magnetron sputtering on 1 cm x 1 cm x 0.5 mm high-resistivity Si substrates ($4.4x10^{14}$ cm^{-3} phosphor-doped). They have a critical temperature (T_c) of 9.2 K, and have an R_s of ~20 μΩ/□ at 4.2 K scaled to 6.5 GHz. The YBCO (~300 nm thick) films have been deposited using planar magnetron sputtering on 1 cm x 1 cm x 0.5 mm $LaAlO_3$ substrate by sputtering deposition. They have a T_c of ~90 K, and an R_s of ~27 μΩ/□ at 4.2 K scaled to 6.5GHz. MgB_2 thin films (~250 nm thick) have been grown by hybrid physical-chemical

vapor deposition (HPCVD) process on 1 cm x 1cm x 0.5 mm sapphire substrate [72]. They have a Tc of ~39 K, and an R_s of ~1.5 mΩ/□ at 4.2 K scaled to 6.5GHz.

The low temperature microwave performance of a wide range of dielectric materials is successfully investigated by PPR technique in this thesis, which includes transition-metal-doped BZT and BZN (ε_r > 20), commercial ultra-pure sapphire (ε_r = ~10), high purity sputtered Si dielectric layers on ultra-pure Si substrate (ε_r = ~11.9), and G-10 fiberglass (ε_r = ~4).

4.2.1.3 Testing of PPR

The PPR measurement configuration inside the Cu cavity is presented in figure 4.4. The cavity is installed at the end of a stainless steel dipping probe, and loaded into a cryostat, Physical Properties Measurement System (PPMS), (Model 6000, QD, San Diego, CA) that can precisely control the magnetic field from 0 to 9 Tesla and temperature from 2 K to 1000 K. The S_{21} and Q-factors are measured by an HP8510 vector network analyzer (VNA). The details of the measurement setup has been reported by Newman and Liu et al [32, 37].

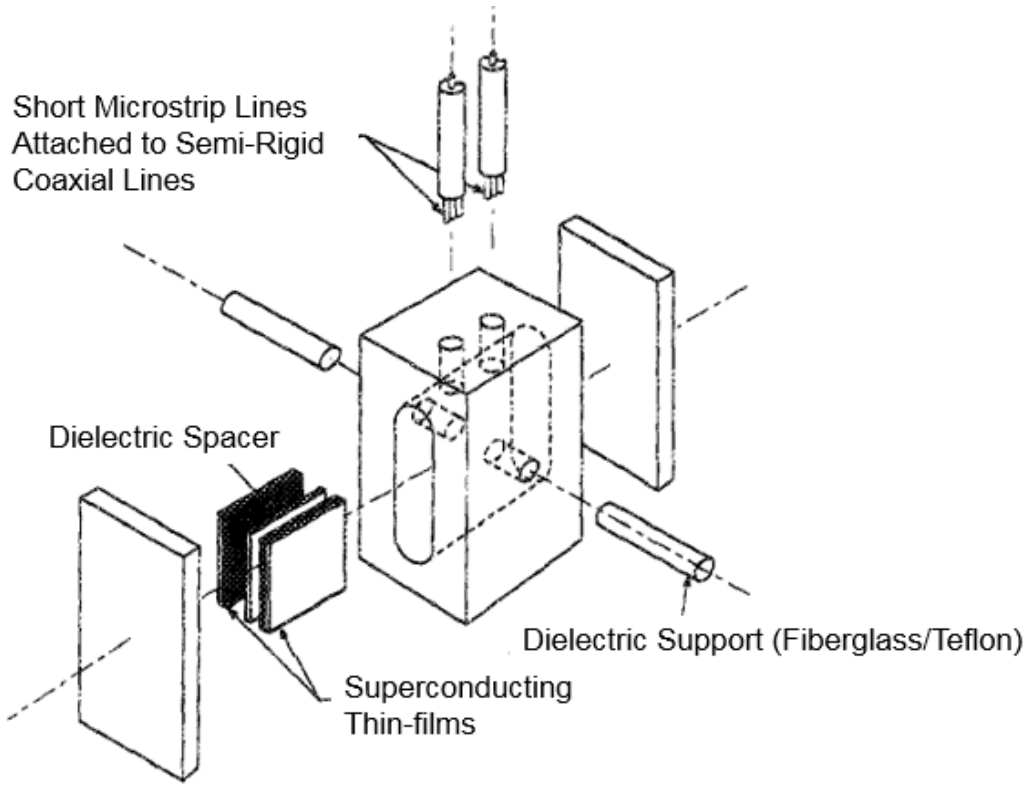

Figure 4. 4 Overview of PPR Testing Configuration [34].

First and foremost, we have to distinguish the PPR resonant peaks from the cavity ones. According to table 4.1, we can see that the measured resonant frequencies match reasonably well with theory and simulation, given the slight difference of boundary conditions and electric probe coupling.

Table 4. 1 An Example of Microwave Measurement results of PPR Using YBCO As the Ground Planes and High Resistivity Si Substrate (0.67 mm Thick) as the Dielectric Layer at 4.2 K.

Resonant Modes	TEM_{10}	TEM_{01}	TEM_{11}	TEM_{20}	TEM_{02}	TEM_{22}
Resonant	5.4335	5.4485	7.9663	10.561	10.906	15.414

Frequency	GHz	GHz	GHz	GHz	GHz	GHz
Q-factor	17440	29410	13610	2769	3944	5609

Fortunately, a superconducting resonator mode can also be easily discerned from a cavity one by measuring the temperature dependence of its resonant frequency. The PPR mode shift has a well-defined temperature dependence associated with the change in the superconductor's penetration depth with temperature [34].

Figure 4.5 shows the characteristic behavior of temperature dependence of fractional frequency shift and Q-factor at the first resonant mode, which validate the resonant peaks are coming from the PPR resonator. The temperature dependence of the fractional frequency shift is calculated using, [f (T) - f(4K)] / f(4K), where f (T) and f (4K) = 5.17823 GHz are the resonant frequency at any given temperature and 4 K, respectively.

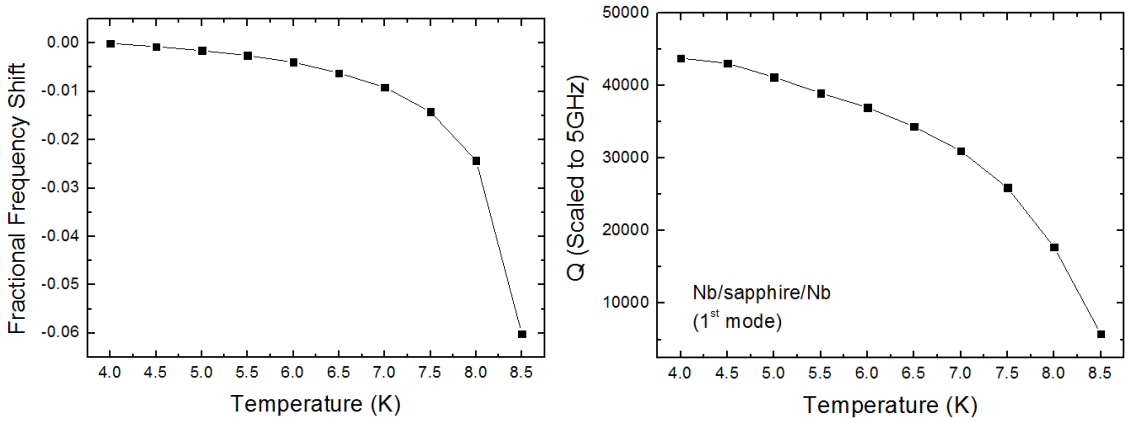

Figure 4. 5 Temperature Dependence of Fractional Frequency Shift and Q-factor (Scaled to 5 GHz) of the First Mode (f_0 = 5.17823 GHz at 4.2 K) in a PPR Resonator Using Nb as Ground Planes and Ultra-pure Sapphire Substrate (0.5 mm Thick) as the Dielectric Layer.

Also, the temperature dependence of the Q-factor can also be used to verify that the mode is the characteristic of the superconductor PPR resonator [34]. We note that the Q-factor of the PPR device decreases as the temperature increases in figure 3.5. When the temperature approaches the superconducting transition temperature (T_c) of Nb, the Q-factor is markedly reduced, and evetually becomes too small to discern near and above T_c. The unloaded Q-factor of a PPR resonator is,

$$1/ Q_{PPR} = \tan \delta + loss_{NF} + \beta R_s/s \qquad \text{Equation (4.2)}$$

where $\tan \delta$ is the loss tangent of the dielectric material in the middle, $loss_{NF}$ is the loss caused by the near-field loss in the cavity, R_s is the surface resistance of superconductor thin films, s is the thickness of the dielectric layer, coefficient β is equal to $1 / \pi\mu_0 f$, where f is the mode frequency and μ_0 is the permeability of free space.

As temperature increases, the normal electron concentration in superconductors increases because the superconducting Cooper pairs are thermally broken, which increases the surface resistance. Thus, according to equation 4.2, the Q_{PPR} will be reduced significantly. The temperature dependence of Q-factors in a Nb-based PPR is shown in figure 3.5, whose trend validates our PPR measurements.

4.2.2 Stripline Resonators

4.2.2.1 Design and Simulation of Stripline Resonator

The Design and simulation of U-shape stripline resonators are discussed in this chapter. Stripline resonator consists of 3 superconducting metal layers and 2 dielectric layers. 2 superconducting ground planes lie on the outside of a narrow superconductor

signal line in the middle, sandwiched by 2 low loss dielectric layers. The configuration is shown in figure 4.6.

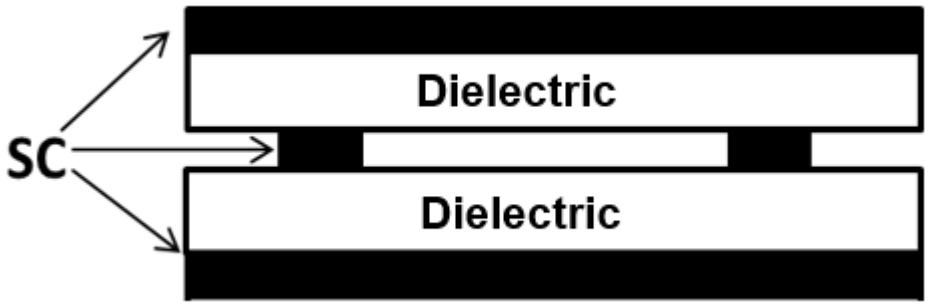

Figure 4. 6 Expanded View of the Cross Section of A Stripline Resonator That is Made of 3 Superconducting (SC) Thin-film Layers, and 2 Dielectric Layers.

To utilize the configuration of our current Cu cavity as a test chamber, a u-shape stripline resonator is designed and its electromagnetic response is simulated using HFSS. The total length of the u-shaped stripline center conductor (s) is 17.8 mm, and the width of the strip is 150 μm. The signal resonates on the stripline in form of standing wave with current form of $I=I_0 \sin(n\pi z/s)$, where n is the mode number, z is the position on the line, and s is the length of the signal line [73]. Because the resonant mode is in the sine wave form, the fundamental mode (f_0) is a half-wavelength electric field pattern, which follows the equation,

$$f_0 = \frac{v}{\lambda} = \frac{c/\sqrt{\varepsilon_r \mu_r}}{2l} = \frac{c}{2l\sqrt{\varepsilon_r \mu_r}} \qquad \text{Equation (4.3)}$$

The fundamental mode (f_0) or first mode (f_1) is calculated to be at 2.44 GHz when Si dielectric materials (ε_r = 11.9 and μ_r = 1) are used. The higher modes, $f_n = nf_0$ (n=2, 3,

4...), so the resonant frequencies of higher modes are at 4.88 GHz, 7.32 GHz, 9.76 GHz, 12.2 GHz…

In HFSS simulation, Si is used for the dielectric layers, and the center conductor and top and bottom ground planes are modeled as a perfect conductor (PEC). The first, second, and third modes are found at 2.34 GHz, 4.73 GHz, and 7.1 GHz, respectively, which matches well with the calculations. The electric fields of the first, second, and third mode are shown in figure 4.7.

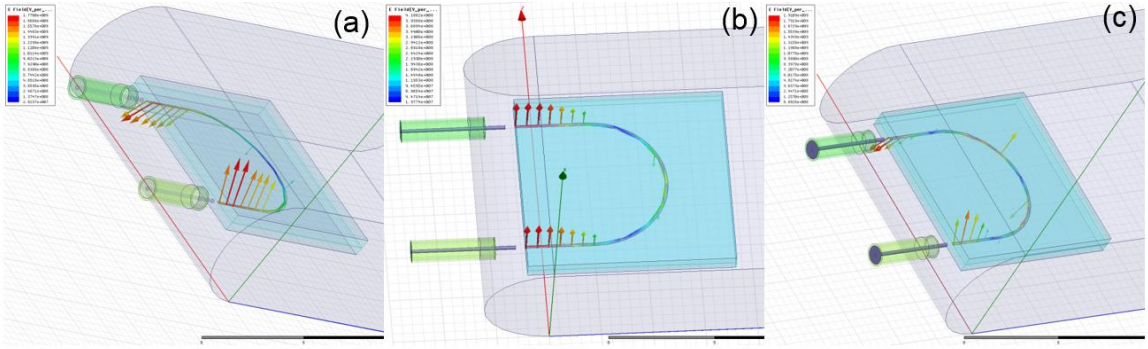

Figure 4. 7 HFSS Simulation of the Electric Fields of (a) First (2.34 GHz), (b) Second (4.73 GHz), and (c) Third (7.1 GHz) Resonant Modes of A U-shape Stripline Resonator, Respectviely.

In figure 4.7, the electric fields at 2.34 GHz show maxima at both ends of the u-shape strip, and minimum in the middle, which verifies a half-wavelength resonant mode. At 4.73 GHz, the electric field vectors indicate that this is a full wavelength mode The electric fields at 7.1 GHz exhibits one and a half-wavelength pattern, consistent with that of a third order mode.

4.2.2.2 Fabrication of U-shape stripline Resonator

1 cm x 1 cm x 300 nm Nb thin films are deposited using planar magnetron sputtering on high-resistivity Si substrates. They have a critical temperature (T_c) of 9.2 K, and have an R_s of ~20 μΩ/□ at 4.2 K scaled to 6.5 GHz. Nb thin-films are patterned into 150 μm wide and 17.8 mm long u-shape strip using standard photolithographic techniques. The Nb pattern is defined by using a Quintel contact mask aligner (Q-2001CT), and etched using reactive ion etching in CF_4 gas.

The YBCO (~300 nm thick) films have been deposited on 1 cm x 1 cm x 0.5 mm $LaAlO_3$ substrate by sputtering deposition. They have a T_c of ~90 K, and an R_s of ~27 μΩ/□ at 4.2 K scaled to 6.5GHz. The YBCO stripline resonator is also patterned by the Quintel contact aligner, and fabricated using wet etch method. The wet etch solution is 0.2 % diluted phosphoric acid.

After the u-shape strip is fabricated, we load the three-piece-stack in the Cu cavity test chamber for microwave measurements at cryogenic temperatures.

4.2.2.3 Testing of U-shape Stripline Resonator

To achieve a reliable and accurate Q-factor measurements with this u-shape stripline resonator technique, the 3 piece stack has to be well-centered in the cavity and the two ends of the u-shape stripline have to align closely to the ends of two coaxial cables to achieve strong coupling.

After the stripline resonator is placed centered in the cavity, the rest of the measurement sequence is the same as that of the PPR and DR techniques, as described in detail previously.

I initially chose Nb as stripline center conductor and ground planes and low-doping concentration Si substrates as dielectric layers, and then measured Q-factors of the 3-piece-stack at 4.2 K in a liquid helium dewar. I found a series of resonant peaks at 2.42 GHz, 4.81 GHz, 9.62 GHz, 12.03 GHz, and 14.43 GHz, which correspond to the first, second, third, fourth, fifth, and sixth mode shown in table 4.2. The measurement results validate the design and simulations of the u-shape stripline resonator performed in HFSS.

Table 4. 2 Microwave Measurement Results of A U-shape Stripline Resonator Using Nb as Ground Planes and High Resistivity Si Substrates (0.5 mm thick) as the Dielectric Layers at 4.2 K.

Resonant Frequency	2.42 GHz	4.81 GHz	7.21 GHz	9.62 GHz	12.03 GHz	14.43 GHz
Q-factor	21,410	8195	5231	4047	7151	4780

Figure 4.8 shows the temperature dependence of fractional frequency shift and Q-factor of the first resonant mode in the superconductor stripline resonator. The results further confirm the existence of resonant modes of a u-shape stripline resonator.

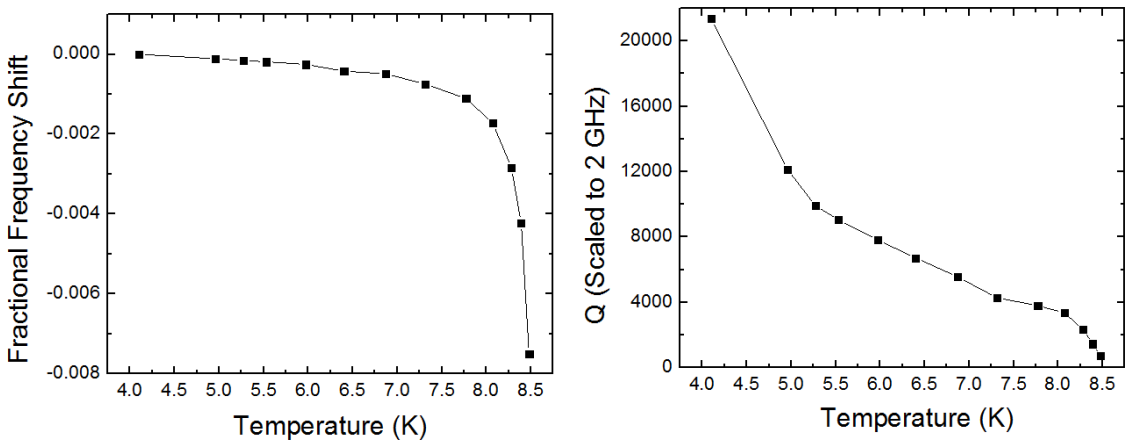

Figure 4. 8 Temperature Dependence of Fractional Frequency Shift of the First Resonant Mode (f_0 = 2.42263 GHz at 4.2 K) and Q-factor of A U-shape Stripline Resonator That is Made of Nb Ground plane / Si Substrate / Nb U-shape Stripline / Si Substrate / Nb Ground Plane.

4.3 Realization of *In-situ* Electron Paramagnetic Resonance (EPR) Spectroscopy

4.3.1 *In-situ* EPR Configuration and Superconductor Electrode Selection

EPR spectroscopy can be used to detect defects with unpaired electrons in an atom, molecule or solid by exposing the material to a monochromatic microwave beam and a varying external magnetic field. In our rendition, we use the dielectric material in a PPR or stripline resonator configuration to generate essentially monochromatic microwaves and then applied a magnetic field parallel to the electrode surfaces. When carrying out this experiment, we found that the surface resistance of the superconductor decreased markedly after being exposed to large magnetic fields, which prevented us from performing accurate and reliable EPR measurements *in-situ*.

The first goal in our experimental work was to identify superconductors whose microwave performance in magnetic fields does not mask the EPR signals of interest. This requires the superconductor losses to not markedly change and be predictable up to

the EPR condition, $B_{ex} = hf_{res} / g\mu_B$, where g is the gyromagnetic ratio of the defect of interest, f_{res} is the resonator's resonant frequency, *h* is the Plank constant, μ_B is the Bohr magneton, and B_{ex} is the static external magnetic field. In this study, low-loss sapphire was used as the dielectric in a parallel plate resonator configuration. As shown in Figure 4.9, we found that YBCO's R_s did not degrade over the fields of interest, while MgB_2 and Nb did. The R_s of Nb and MgB_2 decreases at fields near the measured H_{C1} and drop rapidly thereafter, as would be expected from losses associated with the entrance and subsequent motion of "loose" vortices [73-74]. Since YBCO has the smallest dependence on magnetic field and a higher Tc, we primarily used this electrode for our studies.

The use of Teflon for the resonator support in the cavity was preferable over G-10 fiberglass structures, since the latter introduces a faint EPR resonance at g ~4.35 and linewidth of ~ 30 Gauss due to Fe-contamination, as seen in figure 4.9. This signal was also observed in the fundamental and higher modes of all parallel plate resonators whenever G-10 fiberglass supports were used.

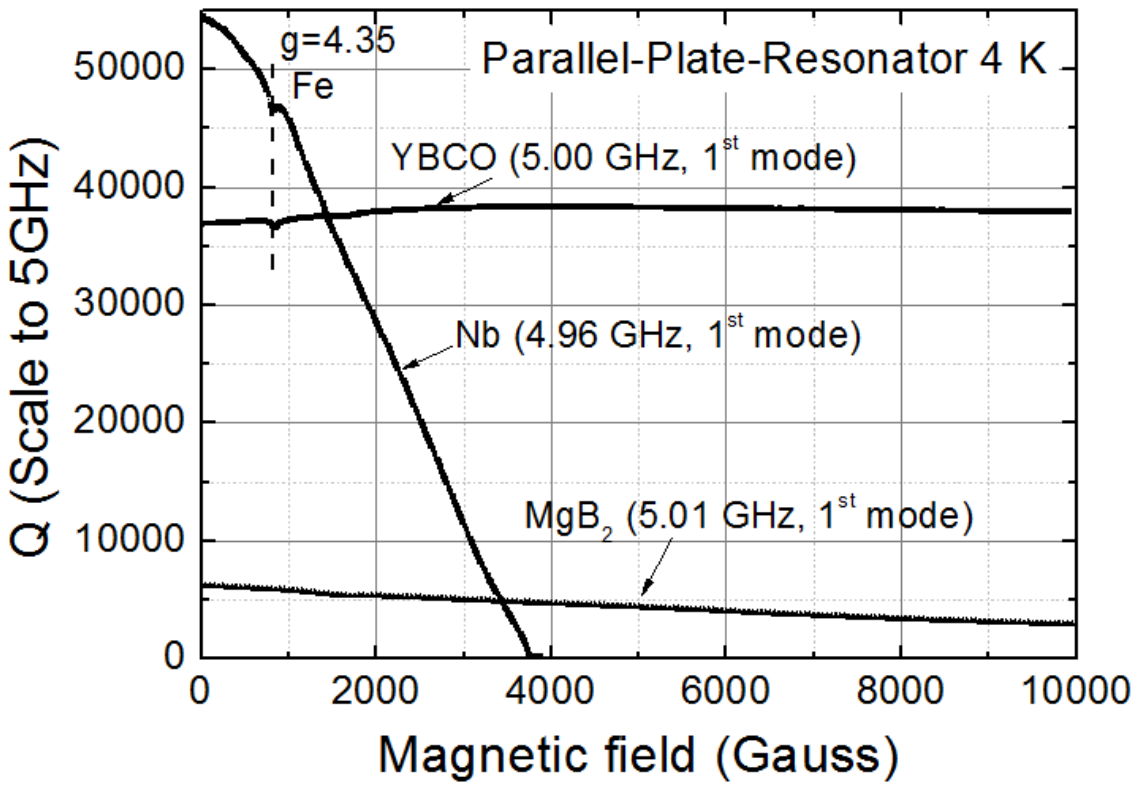

Figure 4. 9 Magnetic Field Dependent Measurements of A PPR Resonator at 4.2 K with Nb, YBCO, and MgB_2 Electrodes and 400 μm Thick Sapphire Substrates. The Fe Signal in the G-10 Fiberglass Supports Is Marked.

4.3.2 Verification of *in-situ* EPR Using PPR Resonators

The introduction of paramagnetic-defects, such as Ni, Mn, and Co, into commercial high-performance microwave dielectrics is commonly done to tune the properties, including the temperature coefficient of resonance frequency [4, 9, 26, 55]. Our earlier study showed that EPR spin excitations dominate the loss at cryogenic temperatures.

Therefore, we chose to study these materials to further optimize the technique and verify the accuracy of our quantitative in-situ EPR superconductor microwave resonator technique. The magnetic field dependent Q measurements of 0.05 at. % Mn-doped BZT

in the parallel plate geometry at temperatures ranging from 4 K to 80 K are shown in figure 4.10. From 80 K to 40 K, we first observed an EPR absorption resonance from 3000 Gauss to 5000 Gauss, with a minimum at ~4210 Gauss. This corresponds to a g-factor of ~2.01, as expected for Mn^{2+} [26, 49, 75-76]. The inset of figure 4.10 shows the first derivative of the data from the 50 K measurement exhibits the six signature Mn^{2+} ($3d^5$) hyperfine EPR peaks [26, 49, 75-76]. When the temperature is less than 50 K, An absorption peak (i.e. Q minimum) centered at ~2050 Gauss is observed, which corresponds to a g-factor of ~4.1. This arises from three dipole-broadened sets of six hyperfine Mn^{2+} EPR peaks [75-76].

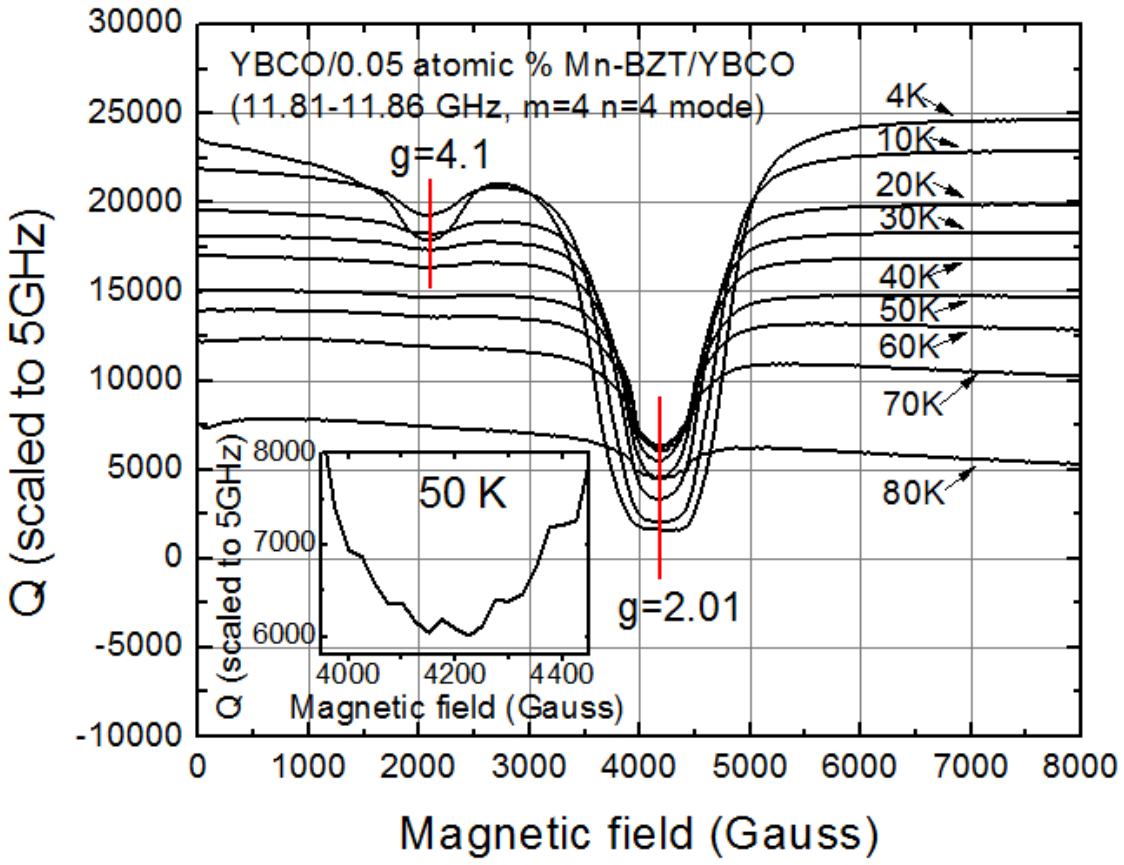

Figure 4. 10 Magnetic Field Dependent Measurements of A PPR Resonator Using YBCO Electrodes and 380 μm-thick 0.05 atomic % Mn-BZT. The Inset Shows the 6 Hyperfine Peaks at g = 2.01 in the 50 K Measurement.

4.3.3 Verification of *in-situ* EPR Using U-shape Stripline Resonators

To test if *in-situ* EPR measurements can be made on stripline resonators, we first used Nb electrodes and a 0.05 atomic % Mn-doped BZT dielectric. We measured the magnetic field dependence of the Q, as shown in figure 4.11 (a). The peak at ~1750 Gauss with 6 hyperfine peaks corresponds to the expected Mn^{2+} g ~2.01 EPR resonance. Next, we measured a stripline resonator with a 0.4 atomic % Co-doped BZN dielectric, whose results are also shown in Figure 4.11 (a). A g-factor of ~4.2 EPR peak was observed at 800 Gauss, characteristic of Co^{2+} in a $Ba(Zn_{1/3}Nb_{2/3})O_3$ lattice [26].

Figure 4.11 (b) shows measurement results for a stripline resonator first with a YBCO electrode and a sapphire dielectric. Then, when the 0.05 atomic % Mn-doped BZT dielectric is measured using the same YBCO stripline, a g = ~2 EPR resonant peak at 960 Gauss is observed with the characteristic Mn^{2+} hyperfine features. Also shown in that figure is a magnetic field dependent measurement of the Q of 0.4 atomic % Co-doped BZN dielectric which exhibits the expected g of ~4.2, the EPR peak of Co^{2+} at ~700 Gauss.

In figure 4.11, we also notice that even without an applied magnetic field, at ambient magnetic field, the Q-factors of the stripline resonators are significantly degraded by the EPR absorption resulting from the transition-metal dopants in the dielectrics.

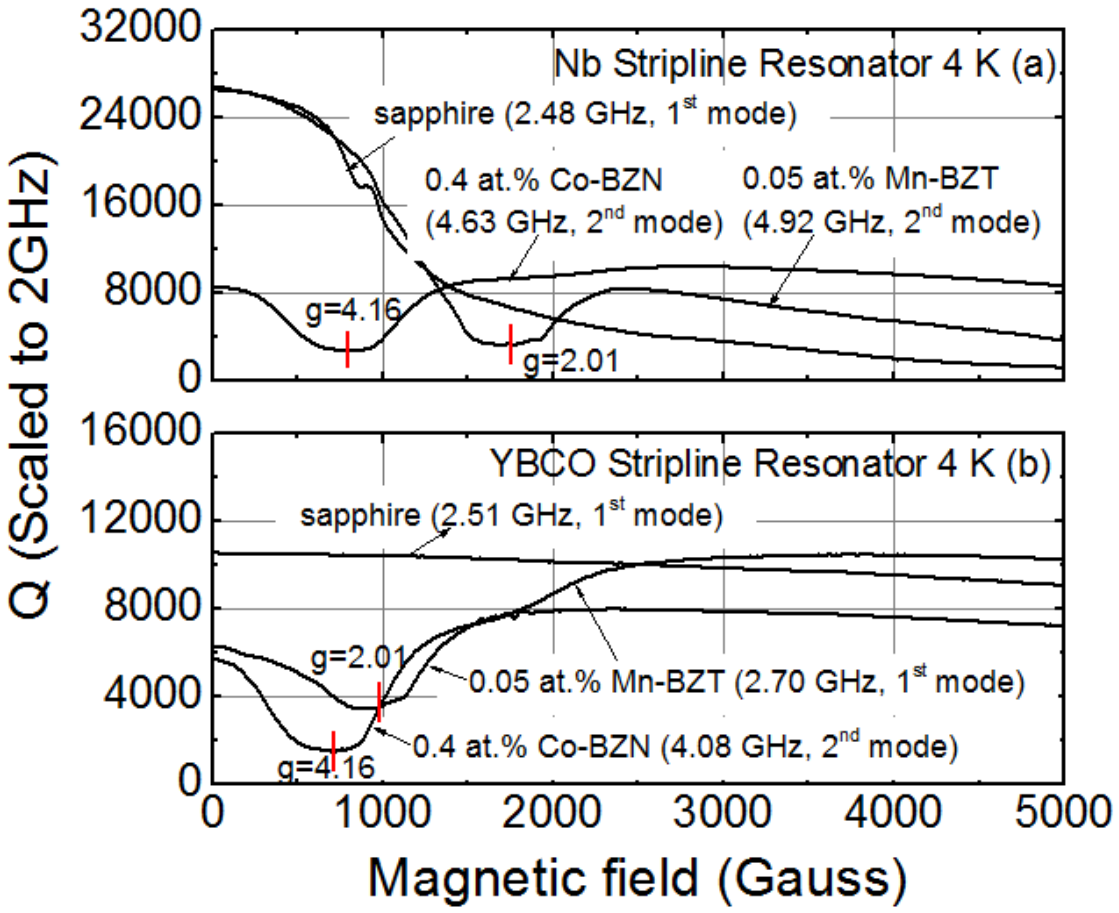

Figure 4. 11 Magnetic Field Dependent Measurement of Q for (a) Nb U-shape Stripline Resonators Using Sapphire, 0.05 at. % Mn-doped BZT, and 0.4 at. % Co-doped BZN at 4.2 K; (b) YBCO U-shape Stripline Resonators Using Sapphire, 0.05 at. % Mn-BZT, and 0.4 at. % Co-BZN dielectrics at 4.2 K.

4.4 Applications of *in-situ* EPR Technique

In the previous sections, we have demonstrated the realization of a new highly-accurate in-situ EPR spectroscopy technique. In this section, we will present the ability of this newly-developed novel technique to (1) identify and quantify the performance-degrading paramagnetic defects in conventional high-purity semiconductors; and (2) to determine the lower critical magnetic field (H_{C1}) in type-II superconductors.

4.4.1 Identification and Quantification of Performance-Degrading Paramagnetic Defects in High-Purity Conventional Semiconductors Using *in-situ* EPR Technique

To investigate the properties of defects in a conventional semiconductor, we performed magnetic field dependent Q measurements on parallel plate resonators with YBCO electrodes and room-temperature-deposited Si on ultra-pure Si substrate, as shown in Figure 4.12. The Si thin-films were deposited using 1500 W DC sputtering at 4.5 kA current in Ar sputter gas. We notice that the resonance peak magnetic field position varies by up to 35 Gauss between cooldowns and when exposed to high magnetic fields. This is characteristic of flux pinning in the electrodes and ground planes, indicating a limiation in accurately determing the g-factor by better than ~2%. To make a direct comparison to convention EPR, a commercial spectrometer (Bruker, ELEXSYS E580, X-band ~9.4 GHz EPR bridge, 1 cm x 2.4 cm cross section, Germany) was used to observe the peak with a g= 2.004 EPR and a similar linewidth of 4.4 Gauss at 4.2 K in the as-deposited Si film. The measured g-factor of 2.004 and linewidth of 4.4 Gauss in our sputtered amorphous Si are not consistent with native defects in Si single crystals [77]. They are, however, similar to the dangling bond defects in (a) sputttered amorphous silicon thin films [78-79] [g=2.0055, linewidth=4.7 Gauss], (b) disordered surfaces of single crystal Si [80] [g=2.0055, linewidth=6 Gauss], and (c) neutron irradiated Si [81] [g=2.0055, linewidth=16-20 Gauss]. This characteristic EPR signal arises from the dangling bonds in clusters of vacancy, interstitials and other native defects [81].

After annealing in an Ar gas at 450 C for 60 minutes, the concentration of these dangling bond defects is decreased below measurable values using our resonator method. Brodsky et al reported that the crystalization temperature is in the range of 450 to 650 C

for amorphous thin-films depending on the film purity, thickness, and substrate materials [77-78].

We determined the density of paramagnetic defects in our measured amorphous Si sample to be 7 x 10^{18} cm^{-3} using a 0.05 atomic % Mn-BZT (Mn^{2+} concentration = 3.9 x 10^{19} cm^{-3}) as a standard. This is believed to provide quantitative answers, given that both samples have similar concentrations and essentially no spin-orbit coupling.

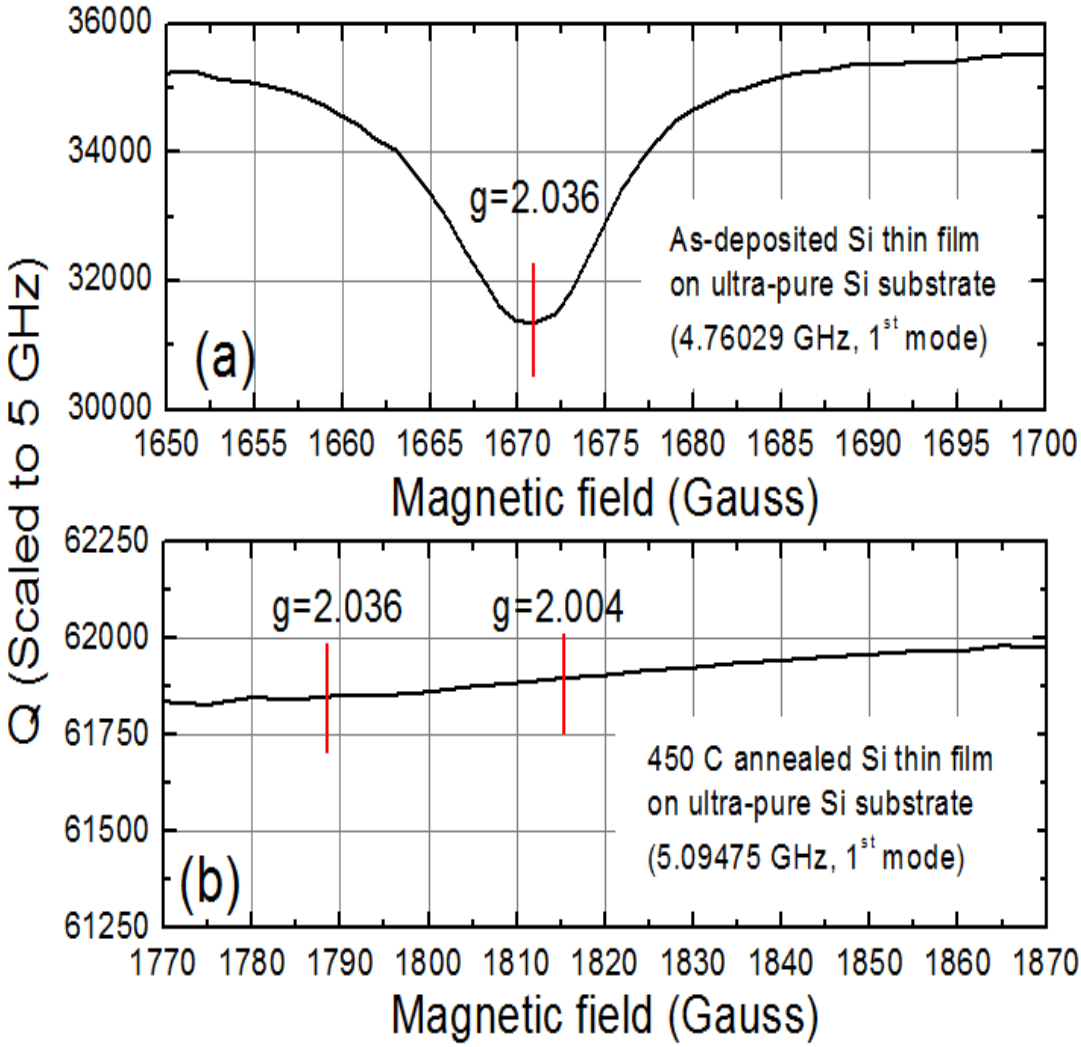

Figure 4. 12 Magnetic Field Dependent Q Measurements of PPR resonators made of YBCO Electrodes and (a) An As-depsoited Si Thin Film on A Ultra-pure Si Substrate Dielectric with An Observable EPR Peak at g=2.0 and (b) a 450 C Annealed Si Thin Film on A Ultra-pure Si Substrate Without A Measureable EPR Peak.

4.4.2 Determination of Lower Critical Magnetic Field (H_{C1}) in Type-II Superconductors Using *in-situ* EPR Technique

4.4.2.1 Introduction of H_{C1} and H_{C2} in Type-II superconductors

In type-II superconductors, when small magnetic fields ($H < H_{C1}$) are applied, the magnetic fields are excluded from superconductors, whose state is called Meissner state.

At this state, superconductors are diamagnetic, so their magnetizations have the same magnitude of the applied magnetic field, but point in the opposite direction. A schematic diagram is shown in figure 4.13 (a). When the applied magnetic fields surpass the lower critical magnetic field, H_{C1}, they enter superconductors in form of magnetic vortices. This state is labeled the mixed state. In the mixed state, the vortex density increases as the magnetic field increases.

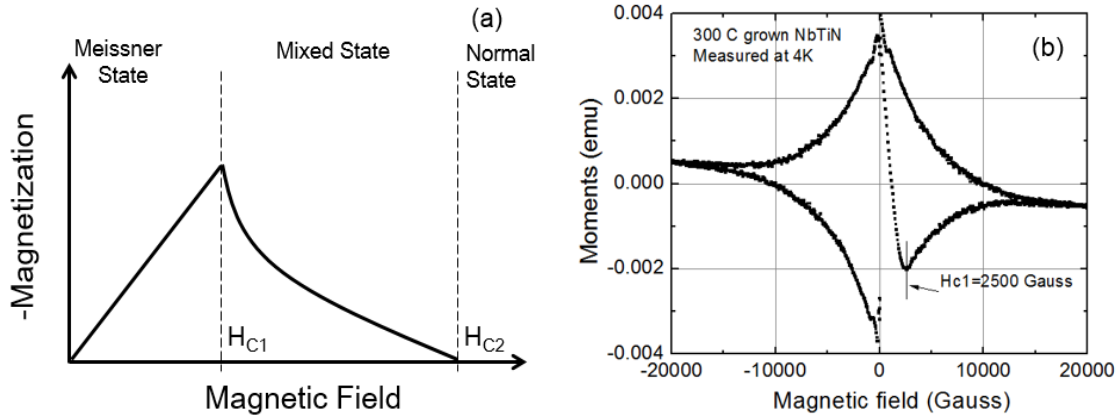

Figure 4. 13 (a) A Schematic of Magnetization as a Function of Magnetic Fields for A Type-II Superconductor, Which Consists of Meissner State, Mixed State, and Normal State. (b) Magnetic Field Dependence of Magnetic Moments of 300 °C Grown NbTiN at 4.2 K, Where the H_{C1} of the Thin Film is ~2500 Gauss and H_{C2} is ~ 20000 Gauss.

Experimentally, H_{C1} and H_{C2} are usually measured by a vibrating sample magnetometer (VSM). H_{C1} of a superconductor is determined at the point in a magnetic field sweep when the magnetization attains the minimum negative moment. The H_{C2} is at the magnetic field where sample's magnetization is nearly zero.

Figure 4.13 (b) shows an example of H_{C1} and H_{C2} determination of a 300 °C deposited NbTiN superconductor thin-film on sapphire substrate at 4 K. The H_{C1} is determined by the magnetic field where the moments reach negative minimum, which is

~2500 Gauss. The H_{C2} is found to be ~20000 Gauss when the magnetization approaches zero and is independent of applied magnetic fields.

4.4.2.2 Determination of H_{C1} in Type-II Superconductors Using *in-situ* EPR Technique

In the previous section, we found that the entry of magnetic vortices introduce additional losses in PPR technique which are associated with the entrance and subsequent motion of unpinned "loose" vortices [73-74]. In stripline resonators, we will show in this section that the sensitivity of the technique to this effect can be even greater.

Figure 4.14 shows the magnetic field dependence of Q-factors for the first mode (2.48 GHz) and second mode (4.91 GHz) in a Nb-based stripline resonator. We observed Q-factor inflection points at ~1000 Gauss for both first and second modes shown in figure 4.14. They both experienced a sharp drop in Q at 1000 Gauss, presumably due to the entrance and subsequent motion of vortices.

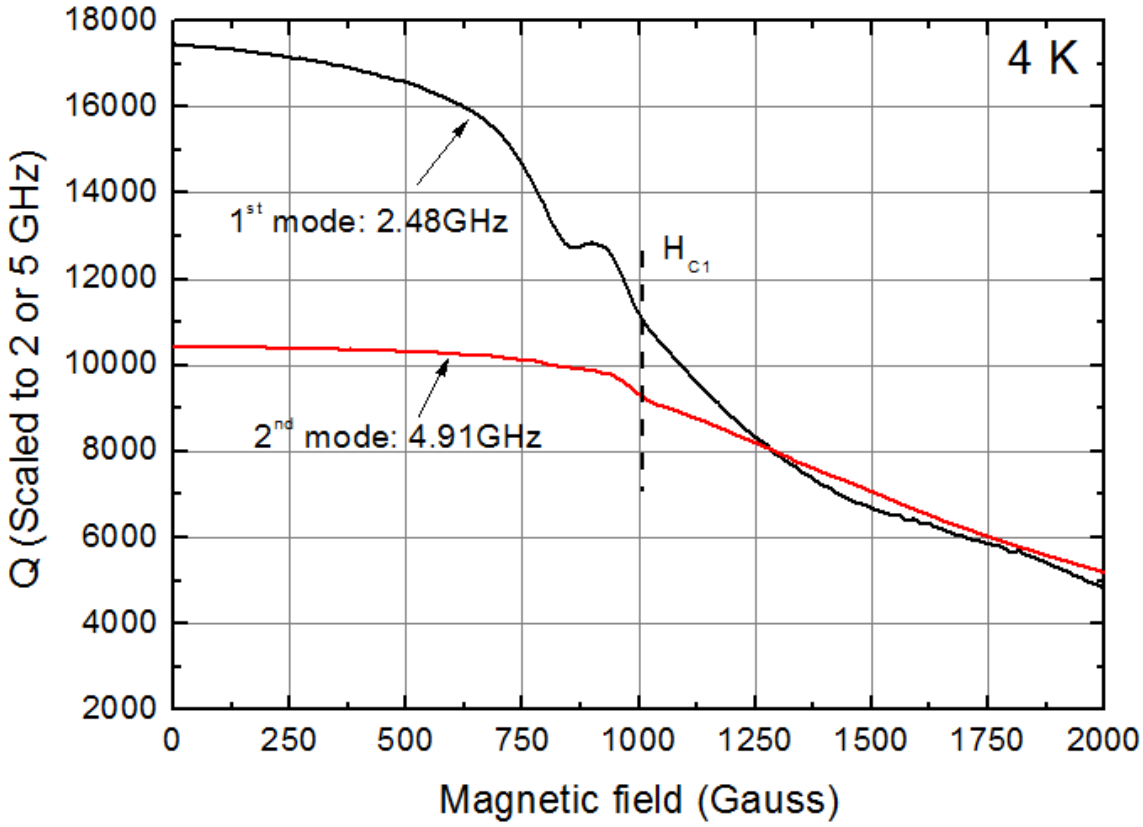

Figure 4. 14 Magnetic Field Dependence of Q-factor Measurements at the First Mode (2.48 GHz) and Second Mode (4.91 GHz) for Nb Striplime Resoantor with Resistive Si Dielectric Substrates. The H_{C1} Marked in the Black Dash Line is Consistent With the Inflection Points in Q-factor Measurements.

To compare to the measurements of H_{C1} made with the most common technique, VSM measurements at 4 K are performed on the same Nb thin-film depsoited on resisitive Si substrate. We found that the H_{C1} (1018 Gauss) measured in VSM is virtually the same as where the Q-factor drop occurred (1005 Gauss), as shown in table 4.3.

Table 4. 3 H_{C1} of Nb Measured by VSM and Q Inflection Points Obtained from the Magnetic Field Dependent Q Measurements of Nb U-shape Stripline Resonator at 3, 4, 5, and 6 K.

Temperature	H_{C1} Measured by VSM	Magnetic Field at Q-factor Inflection Point
3 K	1177 Gauss	1100 Gauss
4 K	1018 Gauss	1005 Gauss
5 K	900 Gauss	915 Gauss
6 K	776 Gauss	760 Gauss

Figure 4.15 shows the same trends for Nb at measurement temperatures from 3 K to 6 K, again consistent with losses from the entry of "loose" vortices motion [73-74]. The magnetic fields where the Q-factor slope change occurs in figure 4.15 are consistent with the H_{C1} values measured by VSM shown in table 4.3, which further validates that this *in-situ* EPR technique can be used to precisely determine the H_{C1} of a superconductor.

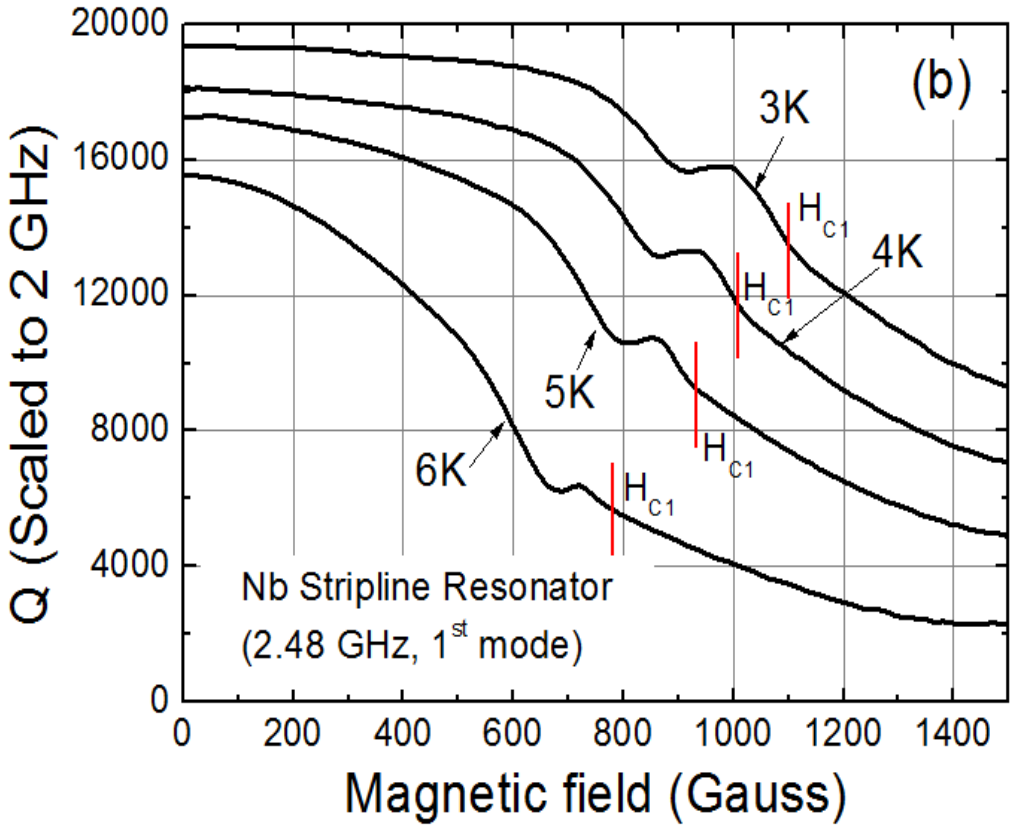

Figure 4. 15 Magnetic Field Dependent Measurements of A Nb Stripline Resonator Using An Ultra-pure Sapphire Substrate as the Dielectric Layer. The H_{C1} of the Nb Thin Film Measured by VSM is Marked by Red Solid Lines.

4.5 Measurement Limitations in *in-situ* EPR Technique

We notice that the resonance peak magnetic field position varies by up to 35 Gauss between cooldowns and when exposed to high magnetic fields. This is characteristic of flux pinning in the electrodes and ground planes, indicating a limitation in accurately determing the g-factor by better than ~2%.

5. SUMMARY

In this work, we first investigated the microwave loss tangents and $\varepsilon_r\mu_r$ in high-k (ε_r = 20 - 40) dielectric materials by performing temperature and magnetic field dependence measurements of Mn, Co, and co-doped Mn-Ni BZT and BZN. It is shown that electron paramagnetic resonance (EPR) absorption process of transition-metals plays a significant and often dominant role in determining the loss tangent at cryogenic temperatures. We also demonstrate that the loss tangent and $\varepsilon_r\mu_r$ follow the Kramers-Kronig relation. It is noteworthy that the Q-factor of 20% Co-doped BZN can be tuned by a factor of over 10, from 1,100 to 12,000 at 10 GHz by controlling a practical magnetic fields at liquid nitrogen temperature.

Then we experimentally determined τ_f, τ_ε, τ_μ and α_L over the temperature range of 2 to 300 K. These results, in combination with DFT calculations, have allowed us to develop a much improved understanding of the fundamental mechanisms responsible for determining τ_f for high-performance microwave dielectrics BZT, 0.8 at.% Ni-doped BZT, and BNT. We find that a Grüneisen analysis using the Debye specific heat model can quantitatively fit the thermal expansion data over the entire temperature range investigated. Our DFT calculations show that from 2 to 300 K, 70% of the observed temperature coefficient of resonant frequency (τ_f) arises from the electronic contribution to the dielectric constant in BZT, in contrast to BNT where virtually the same fraction arises from the phonon contribution to the dielectric constant. At temperatures below 25 K, a Curie dependence from paraelectric defects dominates the temperature coefficient of resonant frequency (τ_f). The magnetic contribution to the temperature coefficient of

resonant frequency (τ_f) in Ni-containing material arises from spin excitations, but is over an order of magnitude smaller than the other contributions.

Lastly, we found that the microwave resonators using YBCO superconductor thin-film electrodes do not show significant Q degradation when a large magnetic field (i.e. < 1 Tesla) is applied parallel to thin films. This resonator device can be used as an *in-situ* electron paramagnetic resonance (EPR) spectroscopy to identify and quantify the concentration of performance-killing point defects in the dielectric. We present the measurements of stripline resonators and parallel-plate resonators made with Mn^{2+} doped $Ba(Zn_{1/3}Ta_{2/3})O_3$ and Co^{2+} doped $Ba(Zn_{1/3}Nb_{2/3})O_3$ high-performance microwave dielectrics, and show that losses are dominated by the EPR absorption from the transition-metal dopants. Very-pure physical vapor deposited Si layers were found to have a concentration of ~7 x 10^{18} cm^{-3} paramagnetic defects, which can be annihilated to below measureable values upon annealing.

REFERENCES

[1] I. M. Reaney and D. Iddles, "Microwave Dielectric Ceramics for Resonators and Filters in Mobile Phone Networks", J. Am. Ceram. Soc., **89**, 2063-2072 (2006).

[2] H. Hughes, D. M. Iddles, and I. M. Reaney, "Niobate-based Microwave Dielectrics Suitable for Third Generation Mobile Phone Base Stations", Appl. Phys. Lett., **79** [18] (2001).

[3] M. T. Sebastian, "Dielectric Materials for Wireless Communication", Elsviser, Linacre House, UK, 2008.

[4] L. Liu, A. Matusevich, C. Gard, and N. Newman, "The Dominance of Paramagnetic Loss in Microwave Dielectric Ceramics at Cryogenic Temperatures", Appl. Phys. Lett., **101**, 252901 (2012).

[5] N. W. Ashroft and N. D. Mermin, "Solid State Physics", Philadelphia, PA, USA, 1976.

[6] E. Iguchi and K. Akashi, "Dielectric Relaxations and Electrical Transport Due to Nonadiabatic Small Polarons in p-Type NiO Doped with Li", J. Phys. Soc. Jap., **61**, 3385-3393 (1992).

[7] O. Bidault, M. Maglione, M. Actis, and M. Kchikech, "Polaronic Relaxation in Perovskites", Phys. Rev. B, **52**, 4191-4197 (1995).

[8] V. B. Braginsky, V. P. Mitrofanov, and V. I. Panov, "Systems with Small Dissipation", University of Chicago Press, Chicago, IL, 1985

[9] L. Liu, M. Flores, and N. Newman, "Microwave Loss in High-performance Dielectric $Ba(Zn_{1/3}Ta_{2/3})O_3$ at 4.2K", Phys. Rev. Lett. **109**, 257601 (2012).

[10] V. L. Gurevich and A. K. Tagantsev, "Intrinsic Dielectric Loss in Crystals", Adv. Phys. **40**, 719-767 (1991).

[11] N. A. Shtin, J. M. L. Romero, and E. Prokhorov, "Theory of Fundamental Microwave Absorption in Sapphire (α-Al_2O_3)", J. Appl. Phys. **106**, 104155 (2009).

[12] E. L. Shirley and H. M. Lawler, "Two-phonon Infrared Spectra of Si and Ge: Calculating and Assigning Features", Phys. Rev. B **76**, 054116 (2007).

[13] T. Shimada, K. Ichikawa, T. Minemura, T. Kolodiazhnyi, J. Breeze, N. M. Alford, and G. Annino, "Temperature and Frequency Dependent of Dielectric Loss of $Ba(Mg_{1/3}Ta_{2/3})O_3$ Microwave Ceramics", J. Eur. Ceram. Soc. **30,** 331-334 (2010)

[14] H. Yabuki, M. Sagawa, M. Matsuo, and M. Makimoto, “Stripline dual-mode ring resonators and their application to microwave devices”, IEEE Trans. Microw. Theory Techn., **44**, 5, 1996.

[15] E. J. Denlinger, “Losses of microstrip lines”, IEEE Trans. Microw. Theory Techn., **28**, 6, 1980.

[16] C.-Y. Chi and G. M. Rebeiz, “Conductor-loss limited stripline resonator and filters”, IEEE Trans. Microw. Theory Techn., **44**, 4, 1996.

[17] S. H. Talisa, M. A. Janocko, C. Moskowitz, J. Talvacchio, J. F. Billing, R. Brown, D. C. Buck, C. K. Jones, B. R. McAvoy, G. R. Wagner, and D. H. Watt, “Low- and high-temperature superconducting microwave filters”, IEEE Trans. Microw. Theory Techn., **39**, 9, 1991.

[18] N. Newman and W. G. Lyons, “High-temperature superconducting microwave devices: fundamental issues in materials, physics, and engineering”, J. Super. **6**, 3, 1993.

[19] P. K. Day, H. G. LeDuc, B. A. Mazin, A. Vayonakis, and J. Zmuidzinas, “A broadband superconducting detector suitable for use in large arrays”, Nature **425**, 817-821, 2003.

[20] R. Barends, J. J. A. Baselmans, J. N. Hovenier, J. R. Gao, S. J. C. Yates, T. M. Klapwijk, and H. F. C. Hoevers, “Niobium and tantalum high Q resonators for photon detectors”, IEEE Trans. On Appl. Super. **17**, 2, 2007.

[21] R. Amsuss, Ch. Koller, T. Nobauer, S. Rotter, K. Sandner, S. Schneider, M. Schrambock, G. Steinhauser, H. Ritsch, J. Schmiedmayer, and J. Majer, “Cavity QED with magnetically coupled collective spin states”, Phys. Rev. Lett. **107**, 060502, 2011.

[22] A. Ghirri, C. Bonizzoni, D. Gerace, S. Sanna, A. Cassinese, and M. Affronte, “$YBa_2Cu_3O_7$ microwave resonators for strong collective coupling with spin ensembles”, Appl. Phys. Lett. **106**, 184101, 2015.

[23] Y. Kubo, F. R. Ong, P. Bertet, D. Vion, V. Jacques, D. Zheng, A. Dreau, J. F. Roch, A. Auffeves, F. Jelezko, J. Wrachtrup, M. F. Barthe, P. Bergonzo, and D. Esteve, “Strong Coupling of a Spin Ensemble to a Superconducting Resonator” Phys. Rev. Lett. **105**, 140502, 2010.

[24] L. DiCarlo, J. M. Chow, J. M. Gambetta, L. S. Bishop, B. R. Johnson, D. I. Schuster, J. Majer, A. Blais, L. Frunzio, S. M. Girvin, and R. J. Schoelkopf, “Demonstration of two-qubit algorithms with a superconducting quantum processor”, Nature, **460**, 240-244, 2009.

[25] K. B. Cooper, M. Steffen, R. McDermott, R. W. Simmonds, S. O, D. A. Hite, D. P.

Pappas, and J. M. Martinis, “Observation of Quantum Oscillations between a Josephson Phase Qubit and a Microscopic Resonator Using Fast Readout”, **93**, 180401, 2004.

[26] S. Zhang, A. Devonport, N. Newman, “Main source of microwave loss on transition-metal-doped $Ba(Zn_{1/3}Ta_{2/3})O_3$ and $Ba(Zn_{1/3}Nb_{2/3})O_3$ at cryogenic temperatures”, J. Am. Ceram. Soc., **98** (4), 1188-1194, 2015.

[27] A. J. Jacobson, B. M. Collins, and B. E. F. Fender, “A Powder Neutron and X-ray Diffraction Determination of the Strucutre of $Ba_3Ta_2ZnO_9$: an Investigation of Pervoskite Phases in the System Ba-Ta-Zn-O and the Preparation of $Ba_2TaCdO_{5.5}$ and $Ba_2CeInO_{5.5}$”, Act Cryst. **B32**, 1083 (1976).

[28] High Frequency Structure Simulator (HFSS) Userguide V.10.0, Ansoft, Pittsburgh, PA, USA, 2005.

[29] D. M. Pozar, "Microwave Engineering", Jogn Wiley & Sons, 4th, New York, USA, 2011.

[30] R. K. Mongia and A. Ittipiboon, "Teoretical and Experimental Investigation on Retangular Dielectric Resonator Antennas", IEEE Trans. Antennas Propag., **45**, 9, 1997.

[31] K. M. Luk and K. W. Leung, "Dielectric Resonator Antennas", Research Studies Press Ltd., PA, USA, 2003.

[32] N. Newman, L. Liu, R. Hanley, and C. Garg, “Resonator Techniques to Characterize Material and Device Properties at Microwave Frequencies in the Quantum Design PPMS Measurement System”, Application note, **40** 1084-750 (2013).

[33] D. Kajfez, “Q-factor Measurements Using MATLAB”, Artech house, Norwood, MA, 2011.

[34] R. C. Taber, "A parallel plate resonator technique for microwave loss measurements on superconductors", Rev. Sci. Instrum. **61**, 2200 (1990).

[35] N. Newman, K. Char, S. M. Garrison, R. W. Barton, R. C. Taber, C. B. Eom, T. H. Geballe, and B. Wilkens, “$YBa_2Cu_3O_7$ Superconducting Films with Low Microwave Surface Resistance over Large Areas”, Appl. Phys. Lett. **57**, 520 (1990).

[36] N. Newman, B. F. Cole, S. M. Garrison, K. Char, and R. C. Taber, “Double Gun Off-Axis Sputtering of Large Area $YBa_2Cu_3O_7$ Superconducting Films for Microwave Applications”, IEEE Transactions on Magnetics **27**, 1276-1279 (1991).

[37] L. Liu, “Mechanisms of Microwave Loss Tangent in High Performance Dielectric Materials”, Arizona State University, Ph.D thesis (2012).

[38] P. W. Anderson and P. R. Weiss, "Exchange Narrowing in Paramagnetic Resonance", Rev. Modern Phys. **25** [1] (1953).

[39] C. Kittel and E. Abrahams, "Dipolar Broadening of Magnetic Resonance Lines in Magnetically Diluted Crystals", Phys. Rev. **90**, 238-239 (1953)

[40] F. Gesmundo and P. F. Rossi, "An EPR Study of Magnetic Interaction in Solid Solutions Between MgO and Antiferromagnetic Oxides. Ⅱ.MgO-MnO", **8**, 297-303 (1973).

[41] J. S. Throp, M. D. Hossain, L. J. C. Bluck, and T. G. Bushell, "Electron Spin Resonance Linewidths of Co^{2+} in Magnesium Oxide", J. Mat. Sci. **15**, 903-908 (1980).

[42] W. Low, "Paramagnetic and Optical Spectra of Divalent Cobalt in Cubic Crystalline Fields", Phys. Rev. **109** [2], (1958).

[43] M. H. L. Pryce and H. H. Wills, "Resonance and Relaxation in Cobalt-doped Magnesium Oxide", Proc. Roy. Soc. (London) **283**, 433 (1965).

[44] K. Dyrek and Z. Sojka, "Coordination and Dispersion of Co^{2+} Ions in CoO-MgO Solid Solutions", J. Chem. Soc. Faraday Trans, **78**, 3177-3185 (1982).

[45] J. S. Throp and M. D. Hossain, "ESR Linewidth Mechanisms in Ni^{2+}/MgO", J. Magnetism and Magnetic Mat. **22**, 311-318 (1981).

[46] D. Gazzoli, M. Occhiuzzi, A. Cimino, D. Cordischi, G. Mineli, and F. Pinzari, "XRS and EPR Study of High and Low Surface Area CoO-MgO Solid Solutions: Surface Composition and Co^{2+} Ion Dispersion", J. Chem. Soc. Faraday Trans. **92**, 4567-4574 (1996).

[47] B. Bleaney and D. J. E. Ingram, "Paramagnetic Resonance and Hyperfine Structure in Four Cobalt Salts", Proc. Roy. Soc. (London), **208**, 143-158 (1951).

[48] A. M. Portis, "Electronic Structure of F Centers: Saturation of the Electron Spin Resonance", Phys. Rev. **91**, 5 (1953).

[49] A. Abragam and B. Bleaney, "Electron Paramagentic Resonance of Transition Ions", Oxford University, UK, p. 124, 1970.

[50] J. H. Van Vleck and V. F. Weisskopf, "On the Shape of Collision-Broadened Lines", Rev. Modern Phys. **17**, 227 (1945).

[51] F. Wooten, "Optical Properties of Solids", Academic press, New York, US, 1972.

[52] P.-F. Ning, L.-X Li, P. Zhang, and W-S Xia, "Raman Scattering, Electronic Structure and Microwave Dielectric Properties of $Ba([Mg_{1-x}Zn_x]_{1/3}Ta_{2/3})O_3$ Ceramics', Ceramics International, **38**, 2, 1391-1398 (2012).

[53] P. K. Davies, J. Tong, and T. Negas. “Effect of Ordering-Induced Domain Boundaries on Low Loss Ba(Zn1/3Ta2/3)O3–BaZrO3 Perovskite Microwave Dielectrics”. J. Am. Ceram. Soc., **80**, 7, 1727-1740 (1997).

[54] K. Endo, K. Fujimoto, and K. Murakawa, “Dielectric Properties of Ceramics in $Ba(Co_{1/3}Nb_{2/3})O_3$-$Ba(Zn_{1/3}Nb_{2/3})O_3$ Solid Solutions’, J. Am. Ceram. Soc., **70**, 9, 215-218 (1987).

[55] G. Rong, N. Newman, B. Shaw, and D. Cronin, “Role of Ni and Zr Doping on the Electrical, Optical, Magnetic, and Structural Properties of Barium Zinc Tantalate Ceramics”. J. Mater. Res. **14**, 10, 4011–4019 (1999)

[56] T. Negas, G. Yeager, S. Bell, and R. Amren, in Chemistry of Electronic Ceramic Materials, Proceedings of the International Conference, Jackson, WY, July 17–20, 1990 (National Institute of Standards and Technology Special Publications, Gaithersburg, MD, 804, 1991).

[57] H. Matsumoto, H. Tamura, and K. Wakino, “Ba(Mg,Ta)O3–BaSnO3 High-Q Dielectric Resonator”, Jpn. J. Appl. Phys., 30, 2347–2349 (1991).

[58] S. N. Gvasaliya, B. Roessli, D. Sheptyakov, S. G. Lushnikov, and T. A. Shaplygina, “Neutron Scattering Study of $PbMg_{1/3}Ta_{2/3}O_3$ and $BaMg_{1/3}Ta_{2/3}O_3$ Complex Perovskites”, Eur. Pyhs. J. B, **40**, 235-241 (2004).

[59] W. Wersing, High frequency ceramics dielectric and their application for microwave components. In: Electronic Ceramics, B. C. H. Steele (Ed.), Elsevier Science Publishers, New York, NY, USA, 1991.

[60] A. R. Akbarzadeh, I. Kornev, C. Malibert, L. Bellaiche, and J. M. Kiat, “Combined Theoretical and Experimental Study of the Low-temperature Properties of $BaZrO_3$”, Phys. Rev. B, 72, 205104, pp1-8 (2005).

[61] R. D. Shannon and C. T. Prewitt, “Effective Ionic Radii in Oxides and Fluorides”, Acta Cryst. B25, 925-946 (1969).

[62] H. W. Willemsen, R. L. Armstrong, and P. P. M. Meincke, “Thermal Expansion Measurements Near the Antiferromagnetic Phase Transition in K_2ReCl_6 and K_2IrCl_6”, 26, 299-309 (1977).

[63] R. P. Lowndes and D. H. Martin, “Dielectric Constants of Ionic Crystals and Their Variations with Temperature and Pressure”, Proc. Roy. Lond. A. 316, 351-375 (1970).

[64] A. T. Fiory, “Electric Dipole Interaction Among Polar Defects in Alkali Halides”, Phys. Rev. B, 4, 2, (1971).

[65] W. Kanzig, H. R. Hart, and S. Roberts, “Paraelectricity and Ferroelectricity Due to Hydroxyl Ions in Alali Halides; Paraelectric Cooling”, Phys. Rev. Lett. 13, 18 (1964).

[66] J. H. Barrett, “Dielectric Constant in Perovskite Type Crystal”, Phys. Rev., 86, 1, 118-120 (1952).

[67] J.-Q. Dai, H. Zhang, and Y.-M. Song, “First-principles Investigation of Intrinsic Dielectric Response in $Ba(B'_{1/3}B''_{2/3})O_3$ with B’ as Transition Metal Cations’, Materials Chemistry and Physics, **159**, 6-9 (2015).

[68] J.-Q. Dai, Y.-M Song, and H. Zhang, "First-principles Study of phonons and Intrinsic Dielectric Response of $Ba(Ni_{1/3}Ta_{2/3})O_3$", Computational Materials Science, **65**, 81-84 (2012).

[69] D. P. Pappas, M. R. Vissers, D. S. Wisbey, J. S. Kline, and J. Gao, “Two Level System Loss in Superconducting Microwave Resonators”, IEEE Trans. On Appl. Super. **21**, 3 (2011).

[70] J. M. Martinis, K. B. Cooper, R. McDermott, M. Steffen, M. Ansmann, K. D. Osborn, K. Cicak, S. Oh, D. P. Papps, R. W. Simmonds, and C. C. Yu, “Decoherence in Josephson Qubits from Dielectric Loss”, Phys. Rev. Lett. **95**, 210503, pp1-3, 2005.

[71] M. Von Schikfus and S. Hunklinger, “Saturation of the Dielectric Absorption of Vitreous Silica at Low Temperatures”, Phys. Lett., **64A**, 1, 1977.

[72] X. H. Zeng, A. V. Pogrebnyakov, A. Kotcharov, J. E. Jones, X. X. Xi, E. M. Lysczek, J. M. Redwing, S. Y. Xu, Q. Li, J. Lettieri, D. G. Schlom, W. Tian, X. Q. Pan, and Z. K. Liu, In situ epitaxial MgB_2 thin films for superconducting electronics, Nat. Mater. 1 **(35),** 2002.

[73] N. Belk, D. E. Oates, D. A. Feld, G. Dresselhaus, and M. S. Dresselhaus, Frequency and temperature dependence of the microwave surface impedance of YBCO thin films in a dc magnetic field: investigation of vortex dynamics, Phy. Rev. B, **53** (6), 1996.

[74] D. Bothner, T. Gaber, M. Kemmler, D. Koelle, and R. Kleiner, Magnetic hysteresis effects in superconducting coplanar microwave resonators, Phys. Rev. B, **86**, 014517, 2012.

[75] J. W. H. Schreurs, Low field hypefine structure in the EPR spectra of Mn2+ containing glass, J. of Chem. Phys., **69**, 2151, 1978.

[76] D. L. Griscom and R. E. Griscom, Paramagnetic resonance of Mn^{2+} in glasses and compounds of the lithium borate system, J. of Chem Phys., **47**, 2711, 1967.

[77] G. D. Watkins and J. W. Corbett, “Electron Paramagnetic Resonance of Defects in Irradiated Silicon”, Discussions Faraday Soc. **31** (86) 1961.

[78] M. H. Brodsky, R. S. Title, K. Weiser, and G. D. Pettit, “Structural, Optical, and

Electrical Properties of Amorphous Silicon Films", Phys. Rev. B, **1** (6), 1970.

[79] M. H. Brodsky and R. S. Title, "Electron Spin Resonance in Amorphous Silicon, Germanium, and Silicon Carbide", Phys. Rev. Lett. **23** (11), 1969.

[80] D. Haneman, "Electron Paramagnetic Resonance from Clean Single-Crystal Cleavage Surfaces of Silicon", Phys. Rev. **170** (3), 1968.

[81] G. K. Walters and T. L. Estle, "Paramagnetic Resonance of Defects Introduced Near the Surface of Solids by Mechanical Damage", J. of Appl. Phys. **32** (10), 1961.

[82] T. Van Duzer and C. W. Turner, "Principles of Superconductive Devices and Circuits", Prentice-Hall. Upper Saddle River, New Jersey, USA, 1999.

APPENDIX

A SUPPLEMENT MATERIALS FOR DENSITY FUNCTION TECHNIQUE (DFT) CALCULATIONS

A.1 Atomic Structure of BZT and BNT for DFT Simulation

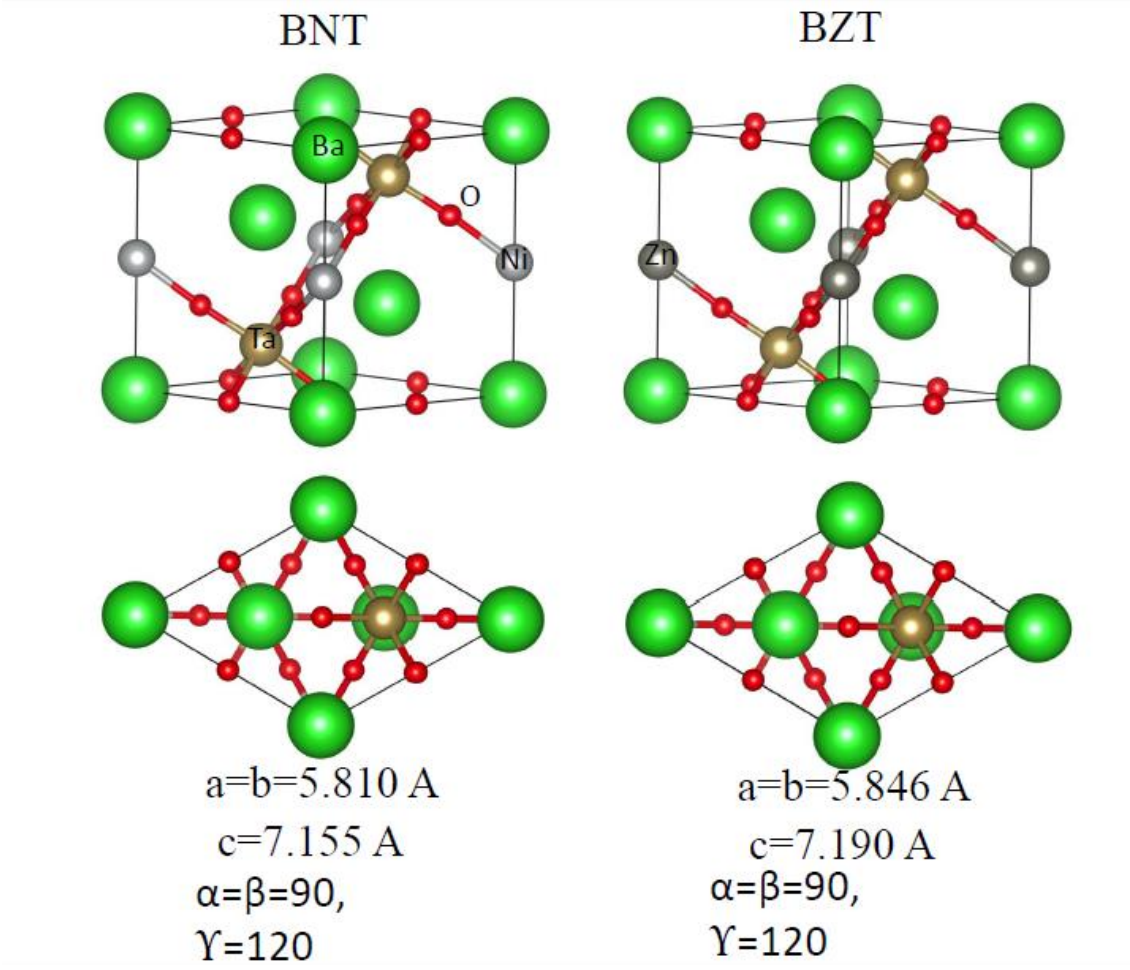

Figure A. 1 Atomic Structure Information of BZT and BNT for DFT Simulation.

A.2 Investigation of Magnetic Order in BNT: Intralayer-ferromagnetic and Interlayer-antiferromagnetic Configuration is the Ground State Because of Its Minimum Energy

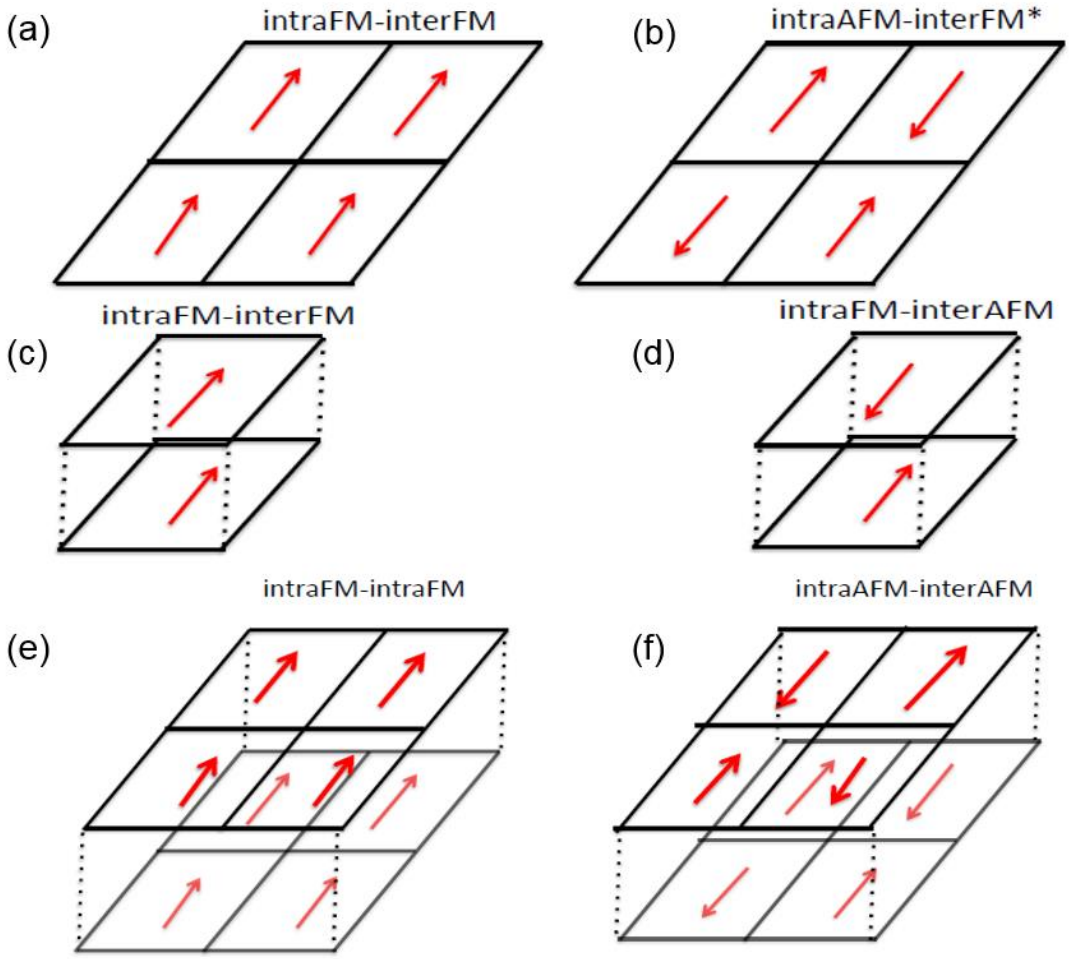

Figure A. 2 (a) and (b) Show That Intralayer-ferromagnetic Configuration is ~0.5 eV Per Unit Cell More Energetically Favorable Than the Intralayer-antiferromagnetic Case when the Interlayer Configuration is Ferromagnetic in a 2 x 2 x 1 Unit Cell; (c) and (d) Show that Interlayer-antiferromagnetic Configuration is 0.003 eV Per Unit Cell More Favorable Than the Interlayer-ferromagnetic Case if the Intralayer is Set to Be Intralayer-ferromagnetic in a 1 x 1 x 2 Unit Cell; (e) and (f) Show That in A 2 x 2 x 2 Unit Cell Intralayer-antiferromagnetic and Intralayer-antiferromagnetic Configuration is 0.011 eV Per Unit Cell More Energetically Favorable Than the Intralayer-ferromagnetic and Intralayer-ferromagnetic One. Therefore, Intralayer-ferromagnetic and Interlayer-antiferromagnetic is the Ground State.

A.3 Interlayer-antiferromagnetic Spin Density Plot of BNT in A 1 x 1 x 2 Unit Cell

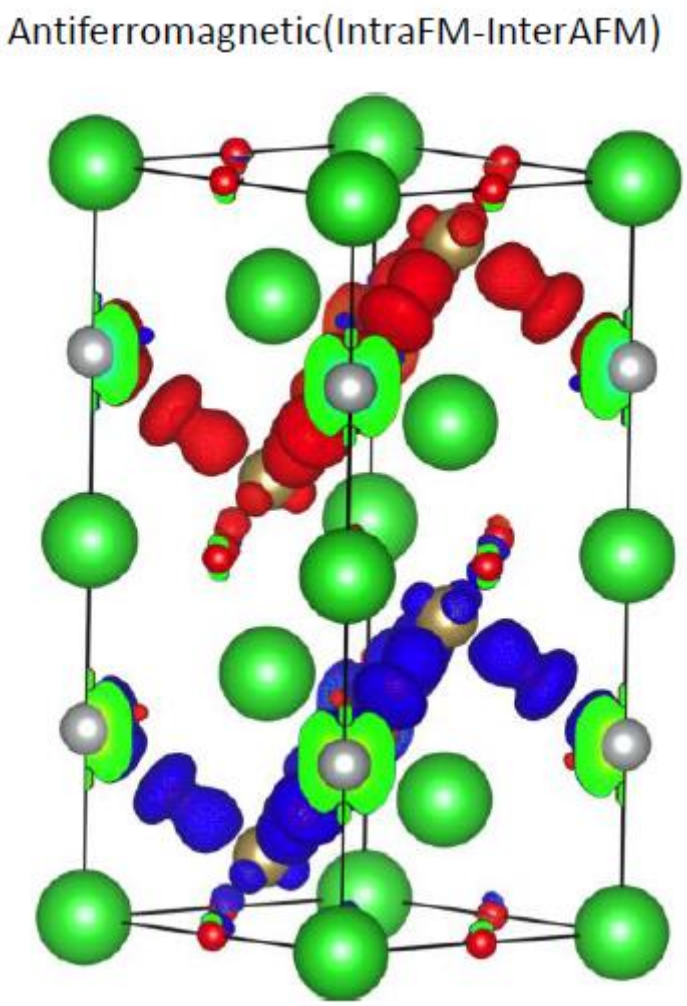

Figure A. 3 Interlayer-antiferromagnetic Spin Density Plot of BNT in A 1 x 1 x 2 Unit Cell. The Red and Blue Charge Densities Represent the Spin-up and Spin-down Ni Spins.

APPENDIX

B KRAMERS-KRONIG MATLAB CODES

B.1 From Imaginary to Real Part:

```
function reeps = kk_itr(omega, imeps)
```

% omega is frequency or magnetic field, “imeps” is the imaginary part of dielectric constant or magnetic susceptibility, “reeps” is the real part of dielectric constant or magnetic susceptibility

```
if(size(omega, 1) > size(omega, 2));
   omega = omega';
end; if(size(imeps, 1) > size(imeps, 2));
   imeps = imeps';
end
g = size(omega, 2);    % size of the vectors
reeps = zeros(size(imeps));    % solution vector initialized

a = zeros(size(imeps));
b = zeros(size(imeps));    % vectors for intermediate calculations

for k = 1:g
   % \/ no principal option
   lemma =  (imeps - imeps(k)) ./ ((omega + omega(k)) .* (omega - omega(k)));
   % lemma = omega .* (imeps) ./ (omega.^2 - omega (k)^2);
   % lemma(k) = 0;
   for p = 1:numel(lemma)
      if(~isfinite(lemma(k))) % quick check to remove singularities
```

```
            lemma(k) = 0;
        end
    end
    reeps(k) = (2 * omega (k)/ pi) * trapz(omega, lemma);
    if(~isfinite(reeps(k)))
        reeps(k) = 0;
    end
  end
end
```

B.2 From Real to Imaginary Part:

```
function imeps = kk_rti(omega, reeps)
% UNTITLED10 Summary of this function goes here
%   Detailed explanation goes here
  if(size(omega, 1) > size(omega, 2));
    omega = omega';
  end; if(size(reeps, 1) > size(reeps, 2));
    reeps = reeps';
  end
  g = size(omega, 2);    % size of the vectors
  imeps = zeros(size(reeps));    % solution vector initialized
  for k = 1:g
    lemma = (reeps - reeps(k)) ./ ((omega + omega(k)) .* (omega - omega(k)));
```

```
        % lemma = (reeps) ./ ((omega.^2 - omega (k)^2));
        % lemma(k) = 0;

        for p = 1:numel(lemma)
           if(~isfinite(lemma(k))) %/ quick check to remove singularities %/
                 lemma(k) = 0;
           end
        end
        imeps(k) = (-2 * omega (k) / pi) * trapz(omega, lemma);

        if(~isfinite(imeps(k)))
           imeps(k) = 0;
        end
     end
end
```